DOE/ER/45574--1

FINAL REPORT

Basic Energy Sciences
Division of Materials Science
Department of Energy
Contract DOE-DE-FG02-96ER45574

THIN FILM ADHESION BY NANOINDENTATION-INDUCED SUPERLAYERS

Submitted by:

Professor William W. Gerberich and Dr. A.A. Volinsky

Department of Chemical Engineering and Materials Science
University of Minnesota
Minneapolis, MN 55455

DISCLAIMER

DISCLAIMER

Portions of this document may be illegible in electronic image products. Images are produced from the best available original document.

TABLE OF CONTENTS

Page

I. PROJECT ABSTRACT

This work has analysed the key variables of indentation tip radius, contact radius, delamination radius, residual stress and superlayer/film/interlayer properties on nanoindentation measurements of adhesion. The goal to connect practical works of adhesion for very thin films to true works of adhesion has been achieved.

II. REVIEW OF ACCOMPLISHMENTS

II.1. Papers and Presentations, 1996–2001

Over 20 publications (or *in press* or submitted) have resulted from this support in this time frame, 13 of which are peer reviewed as listed below. The vast majority of these dealt with various issues in the measurement of adhesion for bilayer or multilayer films:

1. W.W. Gerberich, J.C. Nelson, E.T. Lilleodden, P. Anderson and J.T. Wyrobek, "Indentation Induced Dislocation Nucleation: The Initial Yield Point," *Acta Materialia* **44**, No. 9 (1996) pp. 3585–3598.
2. N.R. Moody, R.Q. Hwang, S. Venkataraman, J.E. Angelo and W.W. Gerberich, "Adhesion and Fracture of Tantalum Nitride Films," *Acta Mater.* **46**(2) (1998) pp. 585–597.
3. D.F. Bahr, J.W. Hoehn, N.R. Moody and W.W. Gerberich, "Adhesion and Acoustic Emission Analysis of Failures in Nitride Films with a Metal Interlayer," *Acta Mater.* **45**(12) (1997) pp. 5163–5175.
4. M.P. de Boer, M. Kriese and W.W. Gerberich, "Investigation of a New Fracture Mechanics Specimen for Thin Film Adhesion Measurement," *J. Mater. Res.* **12**(10) (1997) pp. 2673–2685.
5. M.D. Kriese, D.A. Boismier, N.R. Moody and W.W. Gerberich, "Nanomechanical Fracture Testing of Thin Films," *Engng. Fracture Mech.* **61** (1998) pp. 1–20.
6. D. Kramer, H. Huang, M. Kriese, J. Robach, J. Nelson, A. Wright, D. Bahr and W.W. Gerberich, "Yield Strength Predictions from the Plastic Zone Around Nanocontacts," *Acta Mater.* **47** (1998) pp. 333–343.
7. M.D. Kriese, N.R. Moody and W.W. Gerberich, "Effects of Annealing and Interlayers on the Adhesion Energy of Copper Thin Films to SiO_2/Si Substrates," *Acta Mater.* **46**, No. 18 (1998) pp. 6623–6630.

8,9. M.D. Kriese, N.R. Moody and W.W. Gerberich, "Quantitative Adhesion Measures of Multilayer Films – I. Indentation Mechanics," *J. Mater. Res.* **14**. No. 7 (1999) pp. 3007–3018; II. Indentation of W/Cu, W/W, Cr/W," *ibid.* pp. 3019–3026.

10. N.I. Tymiak, A.A. Volinsky, M.D. Kriese, S.A. Downs and W.W. Gerberich, "The Role of Plasticity in Bimaterial Fracture with Ductile Interlayers," *Metall. and Mat'ls. Trans.* **31A** (1999) pp. 863–872.
11. W.W. Gerberich, D.E. Kramer, N.I. Tymiak, A.A. Volinsky, D.F. Bahr and M.D. Kriese, "Nanoindentation-Induced Defect-Interface Interactions: Phenomena, Methods and Limitations," *Acta Materialia* **47**, No. 15 (1999) pp. 4115–4123.

12. D.E. Kramer, A.A. Volinsky, N.R. Moody and W.W. Gerberich, "Substrate Effects on Indentation Plastic Zone Development in Thin Soft FImls," submitted *J. Mater. Res.* (2001).
13. A.A. Volinsky, N.R. Moody and W.W. Gerberich, "Interfacial Toughness Measurements of Thin Metal Films," submitted *Acta Mater.* (2001).

In addition, 49 presentations were made, the 34 invited being listed below:

Presentations 1996–2001

Associated:

1. With M.P. de Boer, "Adhesion and Spallation of Metal Fine Lines by Microwedge Indentation," Symposium CC 2.7, Spring MRS, San Francisco, April 8, 1996.
2. With D.F. Bahr, J.W. Hoehn and N.R. Moody, "Indentation and Acoustic Emission of Nitrided Films with Metal Layers," 2nd Annual Surface Engineering Symposium, TMS, Cincinnati, October 9, 1996.
3. With M.D. Kriese and N.R. Moody, "Adhesion Assessment of Copper Thin Films," Spring MRS, San Francisco, April 2, 1997.
4. With D.F. Bahr, J.S. Wright, L.F. Francis and N.R. Moody, "Mechanical Behavior of a MEMS Acoustic Emission Sensor,"Materials Research Society Fall Meeting, Symposium I, Materials in Mechanical and Optical Microsystems, 1996.
5. With D.F. Bahr, J.S. Wright, L.F. Francis and N.R. Moody, "The Mechanical Behavior of PZT Thin Films Deposited by a Sol-Gel Technique," TMS Annual Meeting, 1997, Evolution and Advanced Characterization of Thin Film Microstructures.
6. With M.D. Kriese and N.R. Moody, "Effects of Interlayers on the Adhesion of Thin Copper Films," Symposium on Boundaries and Interfaces in Materials III. Fall Meeting TMS, Indianapolis, September 16, 1997.
7. With M.D. Kriese, "Adhesion Measurements of Ductile Copper Thin-Films by Nanoindentation," Symposium NN, Fall MRS, Boston, December 3, 1997.
8. With M.D. Kriese and A.A. Volinsky, "An Improved Method of Thin Film Adhesion Measurement Utilizing Nanoindentation," Symposium T, Spring MRS, San Francisco, April 15, 1998.
9. With N.R. Moody, "Substrate Effects as Determination of Interfacial Fracture Properties," Fall MRS, Boston, December 3, 1998.
10. With Alex Volinsky, "Macroscopic Modeling of the Fine Line Adhesion Test," Spring MRS, San Francisco, April 7, 1999.
11. With Alex Volinsky and Natalia Tymiak, "Deadhesion Properties of Nanocrystalline Films by Nanoindentation," Symposium on Nanocrystalline Materials, Fall Meeting TMS, Cincinatti, OH, November 3, 1999.
12. With Alex Volinsky, "Indentation-Induced Ductile Film Interfacial Debonding," Symposium M, Fall Meeting, MRS, Boston, December 1, 1999.
13. With Neville R. Moody, "Annealing Effects on Interfacial Fracture of Gold-Chrome Films used in Hybrid Microcircuits," Symposium M, Fall Meeting MRS, Boston, December 2, 1999.

14. With Alex Volinsky, "Superlayer Residual Stress Effects on Indentation Adhesion Measurements," Symposium V, Fall Meeting MRS, Boston, December 2. 1999.
15. With Alex Volinsky and others, "Microstructure and Mechanical Properties of Electroplated Cu Thin Films," Fall MRS, Boston, November 29. 2000.

Invited:

16. Invited speaker, "Nanoprobing Coatings for Deformation Resistance and Adhesion," 8th International Coating Process Science and Technology Conference. Spring AIChE, New Orleans, February 27, 1996.
17. Colloquium speaker, "Contact Nanomechanics of Dislocation and Fracture Nucleation," University of Michigan, Ann Arbor, March 22, 1996.
18. Invited speaker, "Nanometer Level Elastic and Inelastic Point Contacts in Thin Films." IMA Mathematical Methods in Materials Science. University of Minnesota, February 8. 1996.
19. Colloquium speaker, "Contact nanomechanics of Dislocation and Fracture Nucleation. Michigan State University, East Lansing, April 23, 1996.
20. Gordon Research Conference on the Science of Adhesion, Invited speaker, "Nanomechanical Probes of Adhered Lines and Films and the True Work of Adhesion," Tilton. NH, August 4. 1996.
21. Invited speaker and symposium organizer, "Nanomechanical Fracture Testing of Phenol-Formaldehyde Thin Films," ICF 9, Sydney, Australia. April 4. 1997.
22. Invited seminar, "Nanoindentation at the Frontiers of Materials Science." Oakridge Chapter of ASM International, May 15, 1997.
23. Invited speaker, "Nanomechanics of Films and Surfaces," Society for Experimental Mechanics, Seattle, Washington, June 3, 1997.
24. Invited speaker, Second Euroconference and International Symposium on Material Instabilities in Deformation and Fracture, "Contact Mechanics of Yield Instabilities," Aristotle University, Thessaloniki, Greece. September 2. 1997.
25. Invited speaker, Gordon Conference on Mechanical Behavior of Thin Films. Plymouth State College, New London, June 23, 1998.
26. Colloquium speaker, "Nanomechanics of Films and Surfaces," Wayne State University, Detroit, Mechanical Engineering, October 5, 1998.
27. Invited speaker, "The Role of Plasticity in Bi-Material Fracture with Ductile Interlayers," Symposium on Composite Interfaces, Fall TMS, Chicago. October 13, 1998.
28. Invited speaker, "Nanoindentation-Induced Defect-Defect Interface Interactions: Phenomena, Methods and Limitations," Acta/Scripta Workshop. La Jolla. October 29, 1998.
29. Invited speaker, "Nanoindentation-Induced Defect-Defect Interface Interactions: Phenomena, Methods and Limitations," Fall TMS, Chicago, November 16. 1998.
30. Invited speaker, "Quantitative Modeling and Measurement of Copper Thin Film Adhesion," Fall MRS Symposium M, Boston, December 3, 1998.
31. Invited paper, "AFM Analysis of Cumulative Fatigue Damage in Cu Thin Films." Spring TMS, San Diego, March 2, 1999.

32. Invited paper, "Acoustic Emission Analysis of Fracture Events in Cu Films with a W Overlayer," Spring MRS, San Francisco, April 7, 1999.
33. Invited speaker, "Nanoindentation Induced Defect Interface Interactions: Phenomena, Methods, and Limitations," Acta-Scripta Workshop, La Jolla, CA. October 29, 1998.
34. Invited speaker, "The Indentation Superlayer Technique for Measuring Thin Film Adhesion," Seminar at NIST, Gaithersburg, November, 16, 1998.
35. Invited speaker, "The Indentation Superlayer Technique for Measuring Thin Film Adhesion," Basic Energy Sciences, Div. Mat'ls. Science, DOE, Germantown. November 18, 1998.
36. Invited seminar, "Local and Global Measures of Adhesion," Macromolecular Science Colloquia, Case-Western University, Cleveland, April 2, 1999.
37. Invited seminar, "True Surface Energies of Film/Substrate Interfaces." Lawrence Berkeley Laboratories, Berkeley, April 9, 1999.
38. Invited colloquium speaker, "Plasticity Effects on Thin Film Adhesion." Materials Science and Engineering Colloquium, Stanford University, Stanford. April 16, 1999.
39. Invited speaker, "The Dislocation Connection Between True and Practical Works of Adhesion," Seminar at NIST, Gaithersburg, June 8, 1999.
40. Invited speaker, "True Surface Energies of Film/Substrate Interfaces." ASME Summer Meeting, Virginia Polytechnic Institute, Blacksburg, June 30, 1999.
41. Invited speaker, "Mechanics of Indentation and Penetration of Materials." Workshop on the Mechanics of Indentation and Penetration, Center for Materials Science, Los Alamos National Laboratory, July 19, 1999.
42. Invited speaker, "The Brittle to Ductile Transition (BDT) in Adhered Thin Films," Symposium V, Fall Meeting MRS, Boston, December 2, 1999.
43. Invited Chair, NSF-Workshop on "Nano and Micromechanics of Solids for Emerging Science and Technology," Palo Alto, October 8, 1999.
44. Invited Departmental Seminar, "Dislocation Nucleation and the Indentation Size Effect," Johns Hopkins University, Baltimore, February 4, 2000.
45. Invited Seminar, "Constitutive Models and Superlayer Techniques for Adhesion Characteristics," Intel Corporation, Hillsboro, OR, February 28, 2000.
46. Invited Seminar, "Thin-Film Adhesion of Cu/X Interfaces," Motorola Inc., Mesa. AZ, July 6, 2000.
47. Invited Colloquium Speaker, University of Illinois, "Challenges in Understanding Small Scale Deformation and Fracture," Urbana Champaign, january 29. 2001.
48. Invited Speaker, with J. Jungk, A.A. Volinsky, J. Vella and I. Adhihetty. "Comparison of Thin Film Adhesion Techniques," Intern. Conf. on Metall. Coatings and Thin Films, Am. Vacuum Soc., San Diego, May 2, 2001.
49. Invited Speaker, "Length Scale Factors in the Adhesion of Al and Cu Films." ASME Symposium on Cu Interconnects and Low k Dielectrics, San Diego. June 28, 2001.

II.2. Significant Findings

From the above investigations a few of the significant findings were:

i) that microscratched induced radial cracking could be utilized to measure fracture toughness of relatively brittle aluminides in the 3 to 15 MPa-$m^{1/2}$ stress intensity range;

ii) during nanoindentation of single crystals or large-grain polycrystals of Fe-3wt%Si GaAs. Cu, Al, W, etc., a yield point could be detected and related to the nucleation event for dislocation emission. These types of measurements are fundamental to several theoretical models as well as the exploration of new alloy compositions where material is of limited availability;

iii) during nanoindentation of single crystals or large-grain polycrystals. arrested yield excursions were shown to be related to dislocation pile-up back-forces of fundamental importance to local work hardening models;

iv) for three types of one- or two-dimensional blisters nucleated by normal indentation or microscratch analysis, a nearly identical adhesion energy of TaN_2 on sapphire was found;

v) For the same evaluation on the same system but with a ductile interlayer. in this case Al, it was found that the interfacial fracture energies decreased. Thus. a very thin ductile interlayer may not be beneficial;

vi) a new type of thin film adhesion test coupon, the precracked fine line scratch test (PLST) was verified to give good measures of fracture toughness;

vii) the three types of evaluation mentioned in (iv) above were also shown to be appropriate for photoresists. Polyimide on Cu provided an order of magnitude more adhesion resistance compared to phenol-formaldehyde on stainless steel:

viii) that a simple relation (from Johnson's contact mechanics) relating plastic zone size to indentation load and yield strength exists even in nanoindentation to a scale on the order of microns. While this can be used to measure the "far-field" yield stress it does not exclude "near-field" indentation size effects. This finding has fundamental impact on how either discretized dislocation or strain-gradient plasticity models for analyzing localized hardening will bridge scale effects:

ix) for measuring yield strength in small volumes, the traditional hardness measure is elevated by a work-hardened flow stress, and sometimes by pile-up. while the Johnson model applied to the elastic-plastic boundary is less so or not at all affected. These measures are relatively independent of the indenter shape as long as the shape-function is appropriately characterized;

x) that a nanoindentation-induced delamination of a bilayer structure provided a rapid, inexpensive measure of thin film adhesion. If proven over a wide range of metal, polymer, semiconductor and ceramic systems, this or something analogous to it could provide quantitative adhesion measures for both fundamental and commercial applications;

xi) that the nanoindentation-induced delamination depended on the superlayer properties, residual stress, indentation depth, delamination radius and film constitutive properties, all of which can be measured by standard (relatively) nanoindentation and wafer bending techniques;

xii) for as-sputtered copper films bonded to SiO_2/Si wafers, the interfacial fracture energy increased by about a factor of 30 (0.6 to 20 J/m^2) as the film thickness increased by about a factor of 30 (100 nm to 3 μm). Annealing the Cu films in one study appeared to slightly increase fracture energies (while in another appeared to slightly decrease fracture energies, calling for additional studies of thermal history effects;

xiii) for the same as-sputtered films a 10 nm titanium interlayer raised the true work of adhesion from 0.6 J/m^2 to 4 J/m^2. Also, the toughness with the interlayer was higher for all Cu thicknesses. Interfacial fracture energies increased from about 4 J/m^2 at 150 nm to 80 J/m^2 at 3 μm, a factor of 20 increase in toughness for a factor of 20 increase in film thickness.

xiv) there appeared to be fracture energy thresholds near a thickness of 100 nm. below which fracture energy decreased no further. This implies that dislocation participation below some threshold associated with the true work of adhesion is nonexistent or of minimal contribution to the energy dissipation.

II.3. Students and Colleagues

J.W. Hoehn (PhD 1996) – Examined corrosion/deformation interactions under both fatigue and fracture loadings. Developed *in situ* TEM and SEM techniques for following dislocation arrays and crack growth rates in NiAl and Fe-3wt%Si single crystals. Is currently a program leader at Seagate Technology, Minneapolis.

M.P. de Boer (PhD 1996; last year support) – Developed the fundamentals for three thin line fracture mechanics test systems for film adhesion: the microwedge indentation test (MWIT), the microwedge scratch tests (MWST) and the precracked fine line scratch test (PLST). The latter is the basis for U.S. Patent Number 5,696,327, December 9, 1997. Is currently a full staff member at Sandia National Laboratories. Albuquerque.

M.D. Kriese (PhD 1998) – Developed the theory and techniques for nanoindentation-induced delamination measures of adhesion. The indentation into a superlayer/metal/substrate system involved comprehensive analysis of composite laminate theory and evaluation of multiple bilayer systems. Is currently a research scientist at Osmic Inc. in Detroit.

A.A. Volinsky (PhD 2000) – Is further developing the theory for superlayer indentation and deconvoluting plasticity, chemical bonding and roughness effects on mode mixity and the work of adhesion.

J. Jungk (new PhD student) – John, having started out on this project will pursue volume/surface area concepts in determining thin film adhesion properties.

Y. Katz (1997–98) – Visiting Professor from the Nuclear Research Establishment. Beer Sheva, Israel. Involved in hydrogen-induced decohesion at bi-material interfaces.

It should be emphasized that three of these students spent pre-doctoral fellowship

awards at Sandia National Laboratories, Livermore for about 3 months each in the time-frame 1995–1997 working with Drs. Michael Baskes and Neville Moody.

III. REVIEW

In addition to the significant highlights and findings reported in Section II, we have prepared a review of this work just submitted to *Acta Materialia*. This is given in the following section.

IV. IMPORTANCE TO THE FIELD

IV.1. Impact on Science and Engineering

A reliable, inexpensive, but also quantitative method for measuring true surface energies in thin films has been the holy grail of adhesion science for more than a decade. Additionally, a similar quest by the engineering community for measures of the practical work of adhesion exists. The proposed test and/or its modification can answer both of these needs. From a theoretical viewpoint, the exciting aspect is to provide quantitative measures which should anchor the fundamental quantities of adhesion. This should allow across-scale connectivity between the lower and upper bounds of interfacial fracture energy, now possible from computational materials science (density functional theory could be applied to clusters of metal/oxide systems for example as it has to platinum/platinum silicide) and quasi-continuum methods. The feedback of such measurements to atomistic and continuum models is essential if the promise of using such simulations in materials design of improved interfaces is to reach fruition.

IV.2. Impact on Industry

All of the above attributes of adhesion measurement (reliable, inexpensive, quantitative) together with "rapid" describe what industry needs for both process development and quality control. While this thin film technique may not be as rapid as a scotch tape test, it is more rapid than a tensile test and the specimen cost is low (in terms of taking a wafer or device off line and sputtering a superlayer on for a quality control measure of adhesion). Such needs are becoming increasingly important as the scale of components size down:

microelectronics industry	:	metal interconnects and polymer photoresists
automotive industry	:	protective metal and paint coatings
print media industry	:	ink-jet printing to polymer protected paper
magnetic recording industry	:	protective DLC (diamond like carbon) films
biomedical devices	:	corrosion and wear resistant films for leads or joint prostheses
biomedical devices	:	MEMS devices based upon shape memory thin films

While not all of these deal with very thin films, we suggest that the technique developed in this study can impact upon all of these billion dollar industries.

INTERFACIAL TOUGHNESS MEASUREMENTS OF THIN METAL FILMS

A.A. Volinsky,† N.R. Moody†† and W.W. Gerberich†††

† Motorola Corp., Mesa, AZ 85202
†† Sandia National Laboratories, Livermore, CA 94551
††† Dept. of Chemical Engineering & Materials Science, University of Minnesota, Minneapolis, MN 55455

ABSTRACT

There are more than 200 different methods for measuring adhesion, suggesting it to be material, geometry and even industry specific. This availability has exploded at least partly due to the arrival of dissimilar material interfaces and thin films and the ease with which microfabrication techniques apply to silicon technology. Having an eye toward those tests utilized for thin films, this paper reviews only a few of these techniques. The emphasis is on measuring thin film adhesion from the standpoint of fracture mechanics, when the film is mechanically or by other means removed from the substrate, and the amount of energy necessary for this process is calculated per unit area of the removed film. This tends to give values approaching the true work of adhesion at small thickness and greater values of the practical work of adhesion at larger thickness, all being in the 30–30,000 nm range. The resulting large range of toughnesses is shown to be dependent on the scale of plasticity achieved as controlled by film thickness, microstructure, chemistry and test temperature.

While the tests reviewed largely address the measurement of elastic strain energy release rates, we also briefly address a few theoretical models which are specific to the resistance side of the delamination equation. The weight of the evidence suggests for ductile metallic films that the major extrinsic variables are film stress, extent of delamination, thickness and temperature while the major intrinsic ones are modulus, yield strength, the thermodynamic work of adhesion and one or more length scales. For some 25 film/substrate multilayers, with emphasis on Al, Au and Cu. the comparison of several theoretical models as to how the extrinsic and intrinsic variable intertwine is made.

NOMENCLATURE

Unless otherwise specified, the following nomenclature is used in this paper:

a	interfacial crack length
A	fracture surface area
b	Burgers vector
C	plastic zone size
c	dislocation free zone
D	diffusion coefficient
d	grain size
E	Young's modulus
E'	plain strain Young's modulus ($E/(1-\nu^2)$)
G	strain energy release rate
Γ_i	interface fracture toughness
H	thin film hardness
h	thin film thickness
J	flux
K	stress intensity at a crack tip ($K_{I,II,III}$ are used for mode I, II and III)
K_C	critical stress intensity of a material
P	load
T	temperature
t	time
U	energy
V_I	indentation volume
W_A	thermodynamic work of adhesion
$W_{A,P}$	practical work of adhesion
σ_{ys}	thin film yield strength
σ	stress ($\sigma_{I,B,R}$ are indentation, buckling and residual stresses respectively)
ϵ	strain, positive taken as compressive
ν	Poisson's ratio
μ	shear modulus

γ	surface energy
Ψ	mode mixity (phase) angle
δ	displacement
Ω	activation volume

SUBSCRIPTS

f	denotes the film
s	denotes the substrate
C or cr	denotes critical
R	denotes residual
$fric$	denotes frictional
I or ind	denotes indentation

INTRODUCTION

Thin film adhesion is a very important property not only for microelectronics and magnetic recording industries, but also for emerging technologies such as data transmission through optical switches which are dependent on microelectromechanical systems (MEMS). In general, films that will adhere to the substrate are desired, though spontaneous delamination may occur at any time due to residual stress induced crack growth between the thin film and the substrate. Qualitative tests such as the scotch tape test or the pull-off test [1,2], are often used to monitor adhesion, since they are quick and easy to perform. While for some applications the formal comparison is good enough, quantitative adhesion values are desired for understanding factors contributing to thin film adhesion, for numerical simulations and lifetime predictions.

Most adhesion tests empirically infer the adhesive strength by subjecting the specimen to some external load and measuring the critical value at which it fails [3]. While still useful for routine quality control, these tests do not measure the interface fracture toughness, since the strain energy release rate usually cannot be deconvoluted from the work of the external load. Linear Elastic Fracture Mechanics (LEFM) is the discipline that provides quantitative answers to specific problems of crack propagation from stresses in different structures. It can be also applied in the case of thin films.

There are a sufficient number of different techniques for measuring thin film adhesion just based on the LEFM approach. However, there are no universal tests for measuring thin film adhesion. This can be explained by the variety of film systems even a single industry (e.g. microelectronic) is dealing with. These represent different types of dissimilar material interfaces that are present in modern electronic device (metal-metal, metal-ceramic, polymer-metal, polymer-ceramic, etc.). As a result, a test that works with one film system may not necessarily work with another. One should also note that adhesion is not a constant, but rather a very complicated variable property, a concept very important for understanding length scale effects in small volumes.

In this paper different adhesion testing techniques will be discussed, along with the fracture toughness results of mostly metal-ceramic interfaces. The emphasis will be on as-deposited thin films, although some thermally treated and/or diffusion-bonded interfaces

will be addressed if these are in the small volume regime arbitrarily defined here as about 10 μm or less. Though there is no standard adhesion test for thin films, there are certain universal approaches that can be applied for measuring film adhesion. However, we must first define adhesion.

DEFINITION OF ADHESION

True Work of Adhesion

From a thermodynamic standpoint *the true work of adhesion* of the interface is the amount of energy required to create free surfaces from the bonded materials:

$$W_A = \gamma_f + \gamma_s - \gamma_{fs} \tag{1}$$

where γ_f and γ_s are the specific surface energies of the film and the substrate respectively, γ_{fs} is the energy of the interface. True work of adhesion is an intrinsic property of the film/substrate pair; that depends on the type of bonding between the film and the substrate, and the level of initial surface contamination.

The true work of adhesion is often determined by contact angle measurements [8,10]. If the tested material particle is in thermal equilibrium on a substrate, then:

$$\gamma_{fs} = \gamma_s - \gamma_f \cos\Theta \tag{2}$$

where Θ is the contact angle between the particle free surface and the substrate (Figure 1).

The work of adhesion now can be expressed with the Young-Dupré equation:

$$W_A = \gamma_f + \gamma_s - \gamma_{fs} = \gamma_f(1 + \cos\Theta) \quad . \tag{3}$$

Droplets in thermodynamic equilibrium can be obtained by the sessile drop method [9] or by annealing [8,10]. In case of the easily oxidized drops such as Cu, annealing must be performed in vacuum. When the surface energy of the film γ_f is known at a given temperature T_0, at any temperature T it would be:

$$\gamma_f(T) \approx \gamma_f(T_0) + (T - T_0)\left(\frac{\partial \gamma_f}{\partial T}\right)_{T=T_0} \quad . \tag{4}$$

Solving eqs. (3) and (4) for the annealing temperature gives the value of *the true (thermodynamic) adhesive energy.* In most of the cases annealing must be performed in vacuum in order to avoid oxidation. If crystallographic faceting occurs upon cooling, a different technique is used to assess the work of adhesion, based on the aspect ratio measurements of the equilibrated crystals [6,7]. Contact angle distribution can be obtained from the SEM or AFM image analysis [8]. Usually both results from contact angle and aspect ratio measurements agree well for metallic films [8].

The true work of adhesion is a constant for a given film/substrate pair, and for metals on ceramic is typically a small number on the order of 0.5–2 J/m^2. Reimanis, *et al.* [7], Lipkin and others [8] measured the thermodynamic work of adhesion of gold on sapphire to be 0.5 to 0.9 J/m^2. Furuya and coworkers calculated adhesive energies of Cu/SiO_2, Cu/TiN and Cu/TiW interfaces using the contact angle technique [10] with the two latter values being more than double the Cu/SiO_2 value of 0.8 J/m^2 as discussed later.

For the idealized case of Griffith fracture [4], the interfacial toughness, Γ_I, is assumed to be equal to the thermodynamic work of adhesion, W_A: $\Gamma_I = W_A$. In practice, even brittle fracture is accompanied by some sort of energy dissipation either through plastic deformation at the crack tip [5], or friction. In this regard, even relatively thin films on the order of 100 nm can exhibit plasticity during interfacial fracture resulting in an elevated work of fracture.

Practical Work of Adhesion

Most of the test methods measure adhesion by delaminating thin films from the substrate. While debonding from the substrate, thin film and/or the substrate usually experience plastic deformation, so it is difficult to extract the true adhesive energy from the total energy measured. What is measured is *the practical work of adhesion*, or interfacial toughness:

$$W_{A,P} = W_A + U_f + U_s + U_{fric} \tag{5}$$

where U_f and U_s are the energy spent in plastic deformation of the film and the substrate, respectively, and U_{fric} is the energy loss due to friction. Although the last three terms appear to be simply additive, it should be noted that both $U_f(W_A)$ and $U_s(W_A)$ are

functions of the true work of adhesion [11] and in many cases $U_{fric}(W_A)$ will be as well. Fracture mechanics approach uses the strain energy release rate, or the crack driving force as a measure of the practical work of adhesion:

$$G \geq R \ , \tag{6}$$

where U is the total energy of the system, and A is the crack area, and R is the resistance to crack propagation. For the films of interest here, the resistance to crack growth is defined as $\Gamma_{(\Psi)}$, the interfacial fracture resistance for mixed mode crack growth. This along with strain energy release rate, as defined for the case of fixed-grips loading (displacement u_0 a constant) condition gives

$$G = -\left[\frac{\partial U_E}{\partial A}\right]_{u_0} \geq \Gamma_{(\Psi)} = R \ . \tag{6a}$$

We first address the tests to determine G, and later consider various resistance terms and several possible ways to interpret that resistance, e.g. phase angle, friction and plastic energy dissipation.

The amount of energy dissipation depends on mode mixity (phase angle), a relative measure of the amount of shear and normal stress components at the crack tip ($\Psi = tan^{-1}(\tau/\sigma) = \tan^{-1}(K_{II}/K_I)$. The concept of mode mixity is presented in Figure 2, which shows that the amount of energy dissipation is higher in pure shear compared to the pure opening fracture mode. Several criteria/phenomenological relationships have been proposed to characterize interfacial fracture energy as a function of the phase angle of loading [16]. There are results in the literature, both experimental and theoretical that exhibit similar behavior [12-16]. The most realistic phenomenological descriptions of the functional dependence of the interfacial toughness on the mode mixity are given by Hutchinson and Suo [16]:

$$\Gamma_{(\Psi)} = \Gamma_0[1 + \tan^2\{\Psi(1-\lambda)\}] \tag{7}$$

$$\Gamma_{(\Psi)} = \Gamma_0[1 + (1-\lambda)\tan^2\{\Psi\}] \ . \tag{8}$$

In these expressions Γ_0 is the mode I interfacial toughness for $\Psi = 0$, and λ is an adjustable parameter (Figure 3). Strictly speaking, there is always a mode mixity effect in the case

of a crack propagating along the interface between two dissimilar materials just due to a mismatch in their elastic properties [17]. Interfacial fracture mechanics considers an interface between two different isotropic materials. In determining fracture toughness through the use of a complex stress intensity factor for bimaterials, this can be expressed as [16]:

$$K = (K_1 + iK_2) = \left(\frac{P}{\sqrt{h}} - i\,\frac{M}{h^{3/2}}\right)\frac{p}{\sqrt{2}}\,h^{i\epsilon}e^{i\omega} \quad , \tag{9}$$

where h is the film thickness, M is the bending moment due to load P, ω is a real angular function $p = \sqrt{(1-\alpha)/(1-\beta^2)}$, and ϵ is a bimaterial real constant:

$$\epsilon = (1/2\pi)\ln[(1-\beta)/(1+\beta)] \quad . \tag{10}$$

The Dundurs parameters α and β for plane strain are [17]:

$$\alpha = \frac{(\mu_1/\mu_2)(1-\nu_1) - (1-\nu_2)}{(\mu_1/\mu_2)(1-\nu_2) + (1-\nu_1)}$$
$$\beta = \frac{1}{2}\frac{(\mu_1/\mu_2)(1-2\nu_2) - (1-2\nu_1)}{(\mu_1/\mu_2)(1-\nu_1) + (1-\nu_2)} \quad . \tag{11}$$

where the μ_i, ν_i are shear moduli and Poisson's ratios for materials 1 and 2. For bimaterials the phase angle Ψ is then defined as follows:

$$\Psi = \tan^{-1}\left[\frac{Ph\sin\omega - 2\sqrt{3}M\cos\omega}{Ph\cos\omega + 2\sqrt{3}M\sin\omega}\right] \quad . \tag{12}$$

The crack path depends on the phase angle, residual stress and the modulus mismatch between the film and the substrate. In the case of a weakly bonded film on a substrate, the interface will be the most likely crack path. There will be cases when the crack can kink either into the substrate or into the film itself [16]. When testing thin film adhesion, knowledge of the fracture interface and the phase angle is necessary in order to interpret the results correctly.

There is also a link between the thermodynamic work of adhesion (W_A) and the interfacial toughness ($\Gamma_{(\Psi)}$). For example, when the thin film yield stress is low, and W_A is high, ductile fracture is the most likely failure mechanism. Conversely, when the film yield stress is high, and the true adhesion is low brittle fracture occurs [8,18–20]. In the

case of a metal film on a brittle substrate, one may improve the interfacial toughness by decreasing the film yield stress (annealing), or by using the interlayers that may increase the W_A term. We will now consider different techniques for measuring the interfacial fracture toughness of thin films.

ADHESION TESTS CLASSIFICATION

There are more than one hundred different methods for measuring thin film adhesion that employ different sample geometries. Some tests use continuous films, some require patterning, but all tests use some driving force or stored energy to achieve thin film delamination. The energy may come from the external mechanical force imposed on the film, or it can be stored in the film itself (through the internal film stress).

Superlayer Test

A test based upon internally developed stresses was proposed by Bagchi and coworkers [21]. Here, residual tensile stresses in a thin film line drive its delamination from a thick substrate. The nondimensional steady state strain energy release rate for a narrow line after crack initiation is:

$$G_{SS}E_f/\sigma_f^2 h_f = 1/2 \quad , \tag{13}$$

where E_f is the Young's modulus of the film, h_f is the film thickness, and σ_f is the residual stress in the film. The corresponding phase angle in this case is about 52° [21]. For the wide line (line width is greater than its thickness) the residual stress is biaxial and the strain energy release rate is:

$$G_{SS}E_f/\sigma_f^2 h_f = 1 - \nu_f \quad , \tag{14}$$

where ν_f is Poisson's ratio of the film. For a typical film thickness of one micron and a residual stress of 100 MPa, the stress-induced energy release rate is too small, on the order of 0.1 J/m^2. As most interfaces in microelectronic devices have higher debond energies, decohesion is difficult if not impossible under these conditions. G_{SS} needs to be increased without substantially changing the phase angle. One of the ways to achieve it is by increasing the resulting film thickness by putting a thick overlayer (superlayer) on top of

the tested structure. For Cu interconnects, Cr was found to be the optimal superlayer [21-22]. The superlayer increases the film total thickness and elevates the total residual stress without changing the tested interface. It is deposited at ambient temperatures (by electron beam evaporation) and does not react with the tested Cu film. More importantly, it has high residual tensile stresses upon deposition. Figure 4 illustrates the test schematically. First a thin carbon release layer is thermally evaporated and patterned using the bilayer photolithography technique. This layer acts like a precrack for the test structure. Its width is at least twice the Cu film thickness to avoid edge effects on the energy release rate.

In the second step the film of interest (Cu) and the superlayer (Cr) are deposited and patterned to form strips perpendicular to the carbon lines. In order to produce a range of strain energy release rates the superlayer thickness is varied. The metal bilayer structure is cut by wet etching or ion milling during the third step. If the strain energy release rate exceeds the adhesion energy, the strips decohere. If the films stay attached, the adhesion energy was not exceeded and a thicker superlayer should be used.

The debond energy G is determined by the critical superlayer thickness [21]:

$$
\begin{aligned}
G &= \sum_i \frac{\sigma_k^2 h_i}{E_i'} - \sum_i \frac{1}{E_i'}\left[\frac{P^2}{h_i} + \frac{12M_i^2}{h_i^3}\right] \\
P &= k\left[\frac{E_1' h_1^3 + E_2' h_2^3}{6(h_1+h_2)}\right] \\
k &= \frac{6(h_1+h_2)(\epsilon_1-\epsilon_2)}{h_1^2 + E_2' h_2^3/E_1' h_1 + E_1' h_1^3/E_2' h_2 + h_2^2 + 3(h_1+h_2)^2} \\
M_i &= E_i' k \quad , \qquad (15)
\end{aligned}
$$

where $i = 1, 2$ refers to the two materials in the bilayer, h_1 and h_2, E_i' are the biaxial elastic moduli, $E_i' = E_i/(1-\nu_i)$, the load P is associated with the residual tension stress, σ_i, in each layer, k is the curvature of the debonded layer, ϵ_i are misfit strains: $\epsilon_i = \sigma_i/E_i'$, M_i are the bending moments along the centerline of each layer due to the load P (Figure 5).

A similar idea of using the superlayer residual stress to drive thin film delamination was employed by Kinbara, *et al.* [23] to debond Ti films with a Ni superlayer. Finite element analysis has been used to calculate the stress distribution in the test structure. As

normal stress was used for the adhesion measurement, the mode mixity effects were not taken into account.

In the case of the residual compressive stress in the line, it may buckle and relieve the stress. The interfacial toughness is calculated then [16,24]:

$$G = \left[\frac{(1-\nu^2)h}{2E}\right](\sigma - \sigma_B)(\sigma + 3\sigma_B) \quad , \tag{16}$$

where σ_B is the buckling stress in Eq. (20), and σ is the stress in the line, which can be calculated from the buckle height, d [16]:

$$\sigma = \sigma_B\left[\frac{3}{4}\left(\frac{d}{h}\right)^2 + 1\right] \quad . \tag{17}$$

Zhuk, *et al.* [26] have measured the practical work of adhesion using the superlayer test and related it to the true work of adhesion from contact angle measurements. Xu, *et al.* [25] used a one μm Cr superlayer with 1 GPa residual stress to form cracks at the end of microlithographed strips.

Though the superlayer test gives accurate adhesion energy values, the testing technique is rather tedious. Several superlayer thicknesses have to be deposited before the lower and upper bounds of adhesion could be extracted. The phase angle is also limited to 50° [21.22]:

Indentation Tests

Nanoindentation is normally used for measuring thin film mechanical properties such as the elastic modulus and hardness [27], which are also useful for modeling the film fracture behavior. In the case of a brittle, weakly bonded film, indentation can be used to delaminate the film from the substrate, thus measure the thin film interfacial strength [29-35]. Basically, the cone (plane stress) and the wedge (plane strain) are the two most popular indenter geometries for measuring brittle thin film adhesion by indentation. Marshall and Evans [29] provide the analysis for the conical indentation-induced thin film delamination. The strain energy release rate is:

$$\frac{GE_f}{(1-\nu_f)} = \frac{1}{2}\, h\sigma_1^2(1+\nu_f) + (1-\alpha)(h\sigma_R^2) - (1-\alpha)h(\sigma_I - \sigma_B)^2 \quad , \tag{18}$$

where E_f and ν_f are the thin film's Young's modulus and Poisson ratio, respectively. h is the film thickness and σ_R is the residual stress in the film. Here, a sharp diamond tip is indented into the tested thin film, and plastically deforms a volume of $2V_I$ (Figure 6(a)). Indentation causes nucleation and propagation of the interfacial crack. If the indenter is driven deep enough, so that the crack reaches its critical buckling length, the film double buckles (Figure 6(b)) during indentation. If the crack length did not reach its critical buckling length on each side of the indenter, single buckling might occur upon tip removal (Figure 6(c)). When the tip is removed, the film under indenter is no longer under constraint, so it may form a single buckle even in the initial double-buckling case.

The indentation stress, σ_I, can be calculated by using the indentation volume, V_I:

$$\sigma_I = \frac{V_I E_f}{2\pi h a^2 (1-\nu_f))} \tag{19}$$

The indentation volume, V_I, can be calculated from the plastic indentation depth using the tip geometry, and the crack length, a, which can be directly measured by using microscopy or profilometry techniques. If the crack is driven far enough by the indenter, the film can buckle, then the Euler buckling stress comes into play:

$$\sigma_B = \frac{\mu^2 h^2 E_f}{12 a^2 (1-\nu_f)} \quad , \tag{20}$$

where μ is a constant, which depends on the boundary condition. The term α is zero if the film does not buckle, and represents the slope of the buckling load versus the edge displacement:

$$\alpha = 1 - \frac{1}{1 + 0.902(1-\nu_f)} \tag{21}$$

Note that in the case of non-buckling fracture ($\alpha = 1$), delamination is only driven by the indentation stress, and the residual stress does not come into play.

A simpler model is presented by Rosenfeld, *et al.* [30] for thick films with low elastic modulus:

$$G = \frac{2(1-\nu_f^2)\sigma_{rx}^2 h}{E_f} \left(\frac{1}{1 + \nu_f + (a/x)^2 (1-\nu_f)} \right)^2 \quad , \tag{22}$$

where σ_{rx} is the radial stress at the indenter contact radius, a is the crack radius and x is the indenter contact radius. If the film hardness, H, is constant through the film thickness,

then the contact radius can be expressed through the indentation load $x = (P/H)^{1/2}$. Applying the Tresca yield criterion, the radial stress σ_{rx} can be expressed through the film hardness H, and the strain energy release rate from Eq. (22) becomes:

$$G = \frac{0.627H^2h(1-\nu_f^2)}{E_f} \frac{1}{[1+\nu_f+2(1-\nu_f)Ha^2/P]^2} \tag{23}$$

The idea of expressing the strain energy release rate is very promising, since the load is continuously recorded during the indentation process, although the model does not account for the thin film residual stress and buckling. It can be applied to relatively thick films (> 10 μm), where hardness does not change with the film thickness and substrate contributions are negligible.

A microwedge wedge indentation test (MWIT) has been proposed by de Boer and Gerberich for thin metal lines [31,32]. Here, a diamond wedge is indented perpendicular to the line to cause its debonding as indicated in Figure 6. An approach similar to [29] is employed, where the plastic volume is assumed to transform into elastic film displacement at the crack tip:

$$G = \frac{E_f' V_0^2}{2b^2ha^2} \quad , \tag{24}$$

where V_0 is half of the total indentation volume, a is the crack length, b is the line width, and E_f' is the plane strain elastic modulus of the film: $E_f' = E_f/(1-\nu_f^2)$. The test accounts for the line buckling, and appropriate solutions are available [31].

A similar wedge indentation test has been applied by Vlassak, *et al.* to measure adhesion of hard films on ductile substrates [34]. It is based on the model for the plane strain wedge indentation into a brittle continuous film on a ductile substrate:

$$G = \frac{(1-\nu_f^2)\sigma_{xx}h}{2E_f} \quad , \tag{25}$$

where σ_{xx} is the stress in the film, perpendicular to the wedge line:

$$\sigma_{xx} = \sigma_R - \nu_f\left(\frac{E_f}{1-\nu_f^2}\right)\frac{W^2\tan\beta}{\pi a^2} \tag{26}$$

Here, σ_R is the residual stress in the film, W is the half width of the wedge indentation, β is the inclination of the face of the wedge to the surface of the film, and a is the crack length.

The advantage of the wedge indenter geometry over conical, Vickers and Berkovich geometries is the stronger $1/a^2$ dependence in Eqs. (24) and (26) compared to $1/a^4$ for the axisymmetric case (Eqs. (18) and (23)). The problem with the wedge indentation is the alignment. Usually, wedges are not perfectly symmetric and difficult to align perpendicular to the plane of the thin film. Misalignment causes asymmetric crack growth on both sides of the wedge. This effect has been observed on both the micro and macro scales [31.36]. A new revision of the wedge indentation test is provided in [37].

A relatively new idea of a cross-sectional indentation test for thin film delamination has been proposed by Sanchez, *et al.* [38]. An indentation is made into the substrate cross-section close to the film interface which causes the film to debond. The energy release rate can be calculated by knowing the maximum film deflection u_0:

$$G = \frac{Eh^3u_0^2}{12(a-b)^2}\,(1-\lambda)^4(2F+\lambda F') \quad , \tag{27}$$

where a and b are the delamination and contact radii, respectively, $\lambda = a/b$, and F is defined as:

$$F(\lambda) = \frac{2\ln\lambda + \frac{1+\lambda}{1-\lambda}\,\ln^2\lambda}{[(1+\lambda)\ln\lambda + 2(1-\lambda)]^2} \quad , \tag{28}$$

and $F' = dF/d\lambda$. This test is particularly useful, as the film is not directly indented, and the crack initiates in the brittle substrate, which limits the amount of plastic deformation.

Unfortunately, indentation tests cannot often be used to test adhesion of ductile films on brittle substrates. A ductile strongly adhered film most often deforms before delamination from the substrate. Even if the film debonds from the substrate, delaminations are not reproducible. However, these problems have been solved with the introduction of the superlayer indentation technique.

Superlayer Indentation Test

Kriese and Gerberich [39] have combined the idea of the superlayer test with the indentation fracture test. Deposition of a highly stressed hard superlayer on top of the film of interest adds additional stress to the delamination process, and prevents out of plane displacements of the film, suppressing plastic pile-up around the indenter. A modified

Marshall and Evans analysis has been used [29], and the laminate theory is employed in order to calculate necessary terms in Eq. (18) for the bilayer [39].

In the case of a highly compressed superlayer, the indentation stress is being added to the residual stress, so multiple superlayer depositions are avoided. Blanket films can be tested in the as-deposited, or as-processed conditions with no pattern transfer necessary. When an indenter penetrates through the bilayer, it causes film debonding and blister formation, which can be viewed in an optical microscope using Nomarski contrast (Figure 7). Properties of the films such as elastic modulus, Poisson's ratio, as well as the tip angle and radius are needed for an adhesion assessment. Generally speaking, there are two measurements that are necessary for strain energy release rate calculations. From the standpoint of blister formation, both indentation depth and blister diameter are required. Blister diameter is measured in the optical microscope with Nomarski contrast. Using the Oliver-Pharr method [27], inelastic indentation depth, δ_{pl}, is calculated from:

$$P = A(\delta - \delta_{pl})^m \quad , \tag{29}$$

where P and δ are the load and displacement from 65% of the unloading slope of the load-displacement curve, respectively. A and m are the power law fitting parameters. Indentation volume, V_I is calculated from the inelastic depth by using tip geometry. Now the indentation stress can be calculated from Eq. (19), assuming the conservation of volume.

The solution for the buckling stress in the bilayer is also provided in [39]. There are two different cases of buckling in the indentation-induced delamination. If the crack is driven far enough, the film may buckle around the indenter when the tip is in contact with the film (double or annular buckling). The film may also buckle back upon the tip retrieval from the film (single buckling), when the total crack length exceeds the critical buckling length. See Figure 6. The appropriate strain energy release rate, G can be determined according to the following rule:

i) $G = G_{nonbuckled}$ if the total stresses in the film never exceed double or single buckling stresses;

ii) $G = G_{nonbuckled}$ if G exceeds G_{single}, but the stress is not sufficient for the double buckling to happen;

iii) $G = G_{double}$ if double buckling occurs and G exceeds G_{single}:

iv) $G = G_{single}$ if none of the above conditions occurs.

Although the residual stress does not come into play if the single film is not buckled (Eq. (18)), the situation may change in the case of a bilayer due to the residual stress in each of the films. The residual stress is typically tensile for a metallic film (Cu, Al, Au, etc.) on a Si wafer mostly due to the thermal mismatch (a metal has a higher thermal expansion coefficient than ceramics). The stress in the superlayer is preferred to be compressive [40]. In the case of a compressive residual stress in the superlayer (W) and tensile stress in the underlayer (Cu), both stresses would contribute to the positive bimaterial beam bending moment, thus the total curvature change (Figure 8). A similar situation has been observed in the case of the bimaterial lines debonding [24]. The fact that the films are bent in the freestanding form means that the critical buckling stress needs to be reduced accordingly to account for the film curvature [41].

The advantage of the superlayer indentation test is that it provides interfacial toughness measurements over a wide range of phase angles. Prior to buckling the phase angle is equal to the real angular function, ω, and at the onset of buckling a rapid decrease occurs.

Scratch Tests

In a typical scratch test a stylus or a diamond tip is drawn across the film surface. The test could be treated as a combination of two operations: normal indentation process and horizontal tip motion. A vertical increasing load is applied to the tip during scratching until the coating detaches from the substrate. The minimum critical load P_{cr} at which delamination occurs is used as a measure of the practical work of adhesion [42,43]:

$$P_{cr} = \frac{\pi r^2}{2}\left(\frac{2EW_{A,P}}{h}\right)^{1/2} , \tag{30}$$

where r is the contact radius and h is the film thickness. This analysis is applicable only when the tensile stress normal to the film surface drives delamination.

Venkataraman, *et al.* developed a model for estimating the energy per unit area G_0 stored in the film from the scratch elastic stress distribution [44,45], which was modified later to account for residual stresses in the film [83]:

$$G_0 = \frac{(1-\nu^2)\sigma_r^2 h}{2E} + \sum\left(\frac{(1-\nu^2)\overline{\tau}_{ij}^2 h}{2\mu} + \frac{(1-\nu^2)\overline{\sigma}_{ij}^2 h}{2E}\right) , \tag{31}$$

where σ_r is the residual stress, $\overline{\tau}_{ij}$ and $\overline{\sigma}_{ij}$ are the average elastic shear and normal stresses in the delaminated film, h is the film thickness, μ is the film shear modulus. $\overline{\tau}_{ij}$ and $\overline{\sigma}_{ij}$ can be determined from the scratch trace geometry observed in SEM.

For a symmetric scratch trace, the strain energy release rate could be found using a circular blister analysis [46]:

$$G_0 = \frac{(1-\nu)h\sigma^2}{E}(1-\alpha)\left(1-\frac{\sigma_B}{\sigma}\right)^2 , \tag{32}$$

where α is defined by Eq. (21) and σ_B is the Euler buckling stress, defined by Eq. (20) for a circular blister with $\mu = \pi$ [16].

In a further development, de Boer, *et al.* adjusted the original scratch test for fine line structures [47,48]. A schematic of this new test. the precracked line scratch test (PLST) is shown in Figure 9. Here, a thin metal line on a substrate is pushed with the asymmetric diamond wedge from its end. For ease of fracture, the thin line has a processed precrack in the form of a carbon layer, which makes it a real fracture mechanics specimen. The carbon layer is similar to that of the superlayer test of Bagchi and Evans [21-22]. The precrack portion of the line is deformed elastically in the beginning of the test until the crack propagates. When the crack reaches its critical buckling length at a certain critical load, P_{cr}, the film buckles. At the point of buckling the strain energy release rate can be calculated as:

$$G = \frac{\sigma^2 h}{2E'_f} = \frac{(P_{cr}-P_{fric})^2}{2b^2hE'_f} \tag{33}$$

Here σ is the stress in the cracked portion of the line, b is the line width, P_{cr} and P_{fric} are the critical buckling load and the friction load, respectively, which are measured experimentally. The test is applicable to relatively hard lines, capable of bearing a load to the crack tip without plastically deforming; it was originally carried out on thin W lines deposited on oxidized silicon wafers. The phase angle just prior to buckling is 52.7°, and decreases rapidly after buckling due to the increased normal stress component. Post-buckling solutions for the strain energy release rate are provided in Refs. 31, 33 and 36. The mechanics for the PLST have been modeled using the macroscopic setup of a polycarbonate line bonded to steel with cyanoacrylate [36]. This allowed a construction of the strain energy

release curve throughout the whole test, before and after the line buckling (Figure 10). Prior to the line buckling an R-curve behavior is observed, when the strain energy release rate increases with the crack length. At the point of buckling there is an unstable crack growth, since the strain energy release rate, G, exceeds the interfacial fracture toughness, $\Gamma(\psi)$ (Figure 11). This situation is analogous to circular blister buckling [16]: at a certain critical level of stress, σ_{buckle}, and a certain crack length, a_1, the line starts to buckle, at which point the interfacial fracture toughness drops under the influence of the phase angle decrease. The crack arrests at a_2 when the strain energy release rate and the interfacial fracture toughness are again in equilibrium. At this point fracture is dominated by the mode I stress component, and continues to grow stably until the total line decoheres [36].

The PLST allows measuring the interfacial fracture toughness over a wide range of phase angles, although it may not be appropriate for ductile metals such as Cu, Al and Au. For this test to work, the material is supposed to transfer the stress down to the crack tip without plastically deforming. This problem may be solved by using a rigid, hard superlayer on top of the film of interest, just like in the superlayer indentation test.

Bulge and Blister Tests

The bulge test is analogous to uniaxial tension for bulk materials and has been developed for measuring mechanical properties of thin films. In the bulge test a freestanding thin film "window" is pressurized on one side, causing it to deflect (Figure 12). A stress-strain curve could be constructed from measured pressure, P, and film deflection δ.

The pressure-deflection curve is a function of sample geometry, its mechanical properties and residual stress. A spherical cap model was initially used for stress and strain determination in the bulge test [49]:

$$\sigma = \frac{Pr^2}{4\delta h} \quad \text{and} \quad \epsilon = \frac{1}{3r^2}\,\delta^2 + A \tag{34}$$

where δ is the total bulge height, h is the film thickness, r is the bulge radius, and A is the term which accounts for initial stress in the film and for slack films is: $2\delta_0/3r^2$, with δ_0 the height due to the slack in the film. For taut films $A = \sigma_0/E'$, where σ_0 is the initial tensile stress in the film, E' is the biaxial modulus of the tested film.

The relation between pressure P and deflection δ may be expressed, based on the cap model:

$$P = \frac{c_1 \sigma_0 h}{a r^2} + \frac{c_2 E h}{r^4 (1-\nu)} \delta^3 \tag{35}$$

where c_1 and c_2 are geometric parameters of the bulge form. Vlassak, *et al.* [49] showed the validity of Eq. (35) for square and rectangular membranes using an energy minimization technique.

The spherical cap model assumes an equibiaxial state of stress and strain in the bulged film, which is not true since the film is clamped and there is no circumferential strain at the edge. There is also an uncertainty in measuring the initial bulge height in the beginning of pressurizing. Finite element analysis was conducted to overcome such problems [49-52] for measurement of biaxial modulus and Poisson's ratio.

Mechanics for the blister test are also given elsewhere [16]. A disadvantage of this method lay in its difficult specimen preparation. If the film is too thin ($< 2\mu$m), it may wrinkle due to the residual stress relief upon being made freestanding [51]. The blister test is similar to the bulge test with the only difference being that the pressure is increased until the film starts to debond from the substrate, forming a blister. The crack extension force (strain energy release rate) for the blister test is given as in [53]:

$$G = P\delta \frac{k_v}{\pi} \left(\frac{4 + 5\phi}{4 + 4\phi} \right) \tag{36}$$

where the coefficient k_v accounts for the shape of the blister and is about 1.62 for a circular window and 1.94 for a square window; ϕ is given as $\phi = \frac{c_2 E'_f}{c_1 \sigma_0} (\delta / r)^2$.

Blister tests are often invalid in the case of thin ductile films due to film yielding before decohesion. In order to prevent film yielding, a hard elastic superlayer may be deposited on top of the film of interest, similar to the superlayer indentation technique. The superlayer can be deposited directly on the freestanding film without causing its wrinkling [54]. Another problem with the blister test is that the crack often does not propagate uniformly along the perimeter of the blister, making it harder to interpret the results. A transition between blister bending and stretching is discussed in [55].

For a homogeneous system the phase angle range in the blister test is between -40 and $-90°$. A comprehensive analysis of mode mixity in the blister test is presented in [56].

Sandwich Specimen Tests

For the sandwich type of test a macroscopic fracture mechanics sample is made with a thin film incorporated into the test structure. This is typically done through diffusion bonding, which can alter both the film microstructure and interfacial adhesion, since the bonding process takes a long time (several hours) and occurs at temperatures close to the melting point. Usually it acts as an annealing step during the sample preparation, which may not be part of a production process. As a result, these types of measurements do not apply to the films in the as-deposited state. These tests are modifications of classical fracture mechanics tests, for which mechanics solutions have been developed. For an isotropic material the crack tends to grow in the opening mode I, but in the case of an interface, the crack tends to grow along the interface. This lends importance to quantification of interfacial fracture toughness as a function of mode mixity.

Many different sandwich sample geometries are possible, so only the most common ones will be considered. The simplest example is the modified K_{Ic} specimen [58,59], where a thin film is bonded between the two pieces of a compact tension sample [57] (Figure 13a). Another version of this test is the double cantilever test, where a thin film is bonded between the two rigid elastic plates. For the K_{Ic} test the interfacial fracture toughness can be expressed in the form:

$$K = \frac{P_Q}{B\sqrt{W}} f(a/W) \quad , \tag{37}$$

where P_Q is the load determined from the load-displacement curve, B is the specimen thickness, W is the specimen width as defined in Figure 13a, $f(a/W)$ is a function of a and W which is defined in the standard for the homogeneous material [57]. McNaney, *et al.* provide the elastic compliance solution for the modified compact tension as well as the four-point bend specimens [60,61].

In the case of the double cantilever test, the strain energy release rate can be expressed as [62,63]:

$$G = \frac{12P^2a_0}{EB^2H^3}[1 + AH/a_0 + B(H/a_0)^2] \quad , \tag{38}$$

where P is the fracture load, a_0 is the precrack length, and H is half the specimen height (Figure 13a), A and B are the proportionality coefficients ($A \approx 1.3$ and $B \approx 0.5$). For

these sandwich specimens, the presence of a thin middle layer does not shift the phase angle much as long as the middle layer is thin compared to the total sample thickness $2H$ [58]. The importance of both tests is that they provide the interfacial toughness for almost pure mode I loading.

Another test, which uses sandwich structure, is the Brazil disk test as shown schematically in Figure 13b. A thin film is bonded in between two pieces of a disk of radius R. A crack of length $2a$ is processed into the interface. Since the load P can be applied at a given compression angle Θ to the crack axis, the mode mixity is varied by changing the angle. Pure mode I conditions are achieved when $\Theta = 0°$ and pure mode II when $\Theta \cong 25°$ [64]. The advantage of the test is the ability to change the phase angle by rotating the sample relative to the axis of the applied load.

Atkinson, *et al.* presented explicit formulae for K_I and K_{II} valid for any crack orientation in the homogeneous Brazil disk [65,66]:

$$K_I = \frac{PN_I}{RB}\sqrt{\frac{a}{\pi}}$$
$$K_{II} = \frac{PN_{II}}{RB}\sqrt{\frac{a}{\pi}} \tag{39}$$

where P is the load applied in compression, a is half the crack length, B is the disk thickness, N_I and N_{II} are non-dimensional functions of the relative crack size, (a/R), and the compression angle Θ. O'Dowd and coworkers provided stress intensity solution for a bimaterial Brazil disk [64]:

$$K = \frac{YP}{2R}\sqrt{2a}(2a)^{-i\epsilon}e^{i\Psi} \tag{40}$$

where Y is a dimensionless geometric factor, ϵ is the bimaterial real constant as in Eq. (10). The dependence of Ψ and Y on the compression angle Θ is not known. Since the crack has two tips, the stress intensity factors at each tip will also be different, so Ψ and Y must be provided for each crack tip. Brazil disk mechanics for orthotropic materials as well as an FEM model are discussed in Ref. [67]. Mechanics for a Brazil-nut-sandwich specimen (Figure 13b) and different failure types are considered in [68].

The last type of the sandwich samples considered here is the four-point bent test [69-72] (Figure 13c). To date this is the most popular adhesion test for the microelectronics

industry. In this test two elastic substrates with thin films on them are bonded together with another material (typically Cu, or epoxy). The upper substrate has a notch in it, and a crack propagates through the substrate and kinks into the interface of interest upon loading. At this point the strain energy release rate reaches steady state, which corresponds to the load plateau in the load-displacement curve. The strain energy release rate can then be calculated from the steady state fracture plateau load P [69] as follows:

$$G = \frac{21(1-\nu^2)P^2L^2}{16Eb^2h^3} \quad , \tag{41}$$

where the geometrical parameters, L, b and h, are shown in Figure 13c. After passing the lower support line, the crack does not exhibit stable growth, and numerical analysis is required to assess G [70]. The phase angle for the test under steady state crack growth conditions is approximately 43° [71]. Limitations of the test in terms of the K-dominance region are discussed in [72].

None of the sandwich specimen tests account for the residual stress in thin films. The ideal test should simulate the practical situation as closely as possible, while also being able to extract the value of practical adhesion. The method must explicitly account for contribution of the residual stress to the decohesion process. If the test structure has experienced only low temperatures upon fabrication, using high homologous temperature (T/T_m) processing steps in specimen preparation, such as diffusion bonding, is not desirable, since it may alter interface adhesion properties.

MECHANICAL PROPERTIES DETERMINATION

For most of the adhesion tests the knowledge of the thin film mechanical properties is required. In the previous section almost every expression for the strain energy release rate has the thin film elastic modulus. The modulus can be measured by the microbeam cantilever deflection technique [73-75], but the easiest way is by means of nanoindentation [27], since no special sample preparation is required and the same technique can be used for measuring film adhesion.

Since there is a contribution of plastic energy dissipation to the fracture process, the maximum amount of this energy would be controlled by the film yield stress. In the case

of a thin film, the yield stress is typically much higher than for a bulk material [76]. This is partly explained by the Hall-Petch type relationship between the film yield stress and its grain size, d:

$$\sigma_{ys} = \sigma_i + kd^{-n} \quad , \tag{42}$$

where σ_i is some intrinsic stress, independent of the grain size d, and n is typically between 0.5 and 1. Since the grain size of a thin film scales with the film thickness, h, the latter can be used instead of the grain size as the scaling parameter [77]:

$$\sigma_{ys} = \sigma_{Cu}[1 + \beta_{Cu}h^{-1/2}] \quad , \tag{43}$$

where σ_{Cu} and β_{Cu} are the fitting parameters, and are 400 MPa and 0.287 $\mu m^{1/2}$ for evaporated Cu films [77].

For a metal film the yield stress can be approximated as 1/3 of the hardness measured by nanoindentation. However, it has been found that for very thin films where penetration depths are small, that the yield strength is often higher than that given by Eq. (43). This has been attributed to either a substrate or indentation size effect [76]. To avoid this, a technique also used is to determine the yield strength by back calculating it from the observed elastic-plastic boundary. That is, it can be extracted from the extent of the plastic zone size around the indenter, C, measured by AFM [76]:

$$\sigma_{ys} = \frac{3P}{2\pi C^2} \tag{44}$$

where P is the applied load. Such yield stress data for sputter deposited Cu films can be found in [78].

Table 1: Yield strength data for sputter-deposited Cu thin films

film thickness, nm	110	200	500	2000
"observed" σ_{ys} †, MPa	650	600	560	450
calculated σ_{ys} ‡, MPa	746	656	562	481

† from Eq. (44) ; ‡ from Eq. (43)

Such a comparison of these yield strengths to those from Eq. (43) are shown in Table 1. While the algorithm used by Wei and Hutchinson [77] gives values about 10 percent higher than "observed," the uncertainty in the elastic-plastic boundary is such that Eq. (43) easily applies to both sets of data.

In a similar way, we have extracted data from aluminum [79] and gold [80,81] films to arrive at similar forms of the algorithm, i.e. for

$$\text{Al}: \quad \sigma_{ys} \simeq \sigma_{\text{Al}}[1 + \beta_{\text{Al}} h^{-1/2}] \tag{45}$$

with a σ_{Al} of 140 MPa and a β_{Al} of 0.8 $\mu\text{m}^{1/2}$ and for

$$\text{Au}: \quad \sigma_{ys} \simeq \sigma_{\text{Au}}[1 + \beta_{\text{Au}} h^{-1/2}] \tag{46}$$

with a σ_{Au} of 315 MPa and a β_{Au} of 0.287 $\mu\text{m}^{1/2}$. With these yield properties established and using accepted values of 70 GPa, 80.8 GPa and 120 GPa for Young's moduli of Al, Au and Cu, we will proceed to present thin film adhesion data mostly concentrated on these three systems. Note that the 120 GPa modulus for Cu is slightly less than its bulk value due to porosity.

THIN FILM ADHESION

With the ability to measure interfacial fracture resistance and yield strength using the many test techniques reviewed, it was next appropriate to examine such thin metallic film properties. The following first involves providing data from a broad number of sources, principally focused on as-deposited thin films but some from buried and/or diffusion bonded films for comparison [8,10,27,24,25,38,46,71,80–103].

All of these data collected for films mostly below several microns thick are given in Table 2. It is seen that the data are concentrated on Al, Au and Cu systems although a few dealing with other FCC and BCC metal systems are given at the bottom. For the arrows under the yield column these refer to a range of yield strength corresponding to Eqs. (43), (45) and (46) for the range of thicknesses studied. The two exceptions are for the Cu/SiO_2 interfaces where for thicknesses of 80 nm and 500 nm, a range of yield strengths were obtained as a function of test temperature. What follows are a short descriptive account

of the interfaces associated with the three main metallic films studied. Subsequently, several mechanisms and models which address nonlinear deformation contributions are briefly reviewed and compared to these data.

Aluminum Films

Most of the thin film adhesion data [25,71,87,89,101,102] have been generated using either superlayer indentation [39] as in Figure 7, or the four-point bend UCSB test [69–72] as in Figure 13c. In all cases substrates were silicon wafers with SiO_2 between the silicon and deposition layer(s) or sapphire wafers. For the superlayer indentation tests, either W or Ta_2N superlayers on the order of 1 μm thick were used incorporating a residual stress on the order of 1 GPa compression or 100 MPa tension. Within the data scatter, a small effect of residual stress was found on the resulting adhesion measurements. Three types of interfaces were evaluated, a direct deposit of Al, one with 40 nm of carbon as an interlayer and one with 40 nm of copper as an interlayer [101,102]. The latter two were known to provide lower adhesion. For 500 nm thick films these provided G_c values of 8.0, 0.65 and 0.6 J/m^2. These are consistent with values determined by Schneider, *et al.* [87] using the same type of test but with a Ta superlayer and 500 nm of Al on Al_2O_3. Here, without and with carbon as a contaminant, the toughness was 5.6 and 1.05 J/m^2. Another consistent result, even with using a different test, was found by Dauskardt, *et al.* [71] on Al-Cu depositions with a 120 nm thick TiN/Ti/TiN innerlayer. For a 500 nm film their interpolated value would be 8.5 J/m^2. In another study using a thinner 70 nm TiN/Ti/TiN innerlayer, Xu, *et al.* [25] found the TiN/SiO_2 interface failure energy to be on the order of 1.9 J/m^2 in the absence of humidity effects. Both Volinsky, *et al.* [101,102] and Dauskardt, *et al.* [71] ran evaluations over a range of thicknesses with the average values of all data without contaminants from Table 2 being summarized in Figure 14. Irrespective of the strong innerlayer or whether the substrate is SiO_2/Si or Al_2O_3, there is a consistent increase in fracture resistance from about 4 J/m^2 to 12 J/m^2 with an order of magnitude increase in thickness from 200 to 2000 nm. It appears then that for strong interfaces, the measured strain energy release rate is dominated by the aluminum thickness in Al/X_i/SiO_2 or Al/X_i/Al_2O_3 systems as long as all X_i innerlayers are reasonably thin. Note that this would apply equally to Al or Al-Cu films.

Gold Films

To our knowledge, Au films have been studied exclusively on Al_2O_3 substrates or as bonded interfaces between sapphire slabs [84,92,93]. In the former either telephone cord blister analysis [16] or the superlayer indentation test used TaN as the superlayer. The bonded interface was evaluated as a double-cleavage drilled compression test which is similar to the Brazil disk test loaded along the crack line. See Lipkin, *et al.* [8] and Turner and Evans [84] for more details. While a methodical study of thickness variations has not been completed one can surmise that there is a large effect since a two order of magnitude increase in thickness variation in the two studies (0.2–15 μm) resulted in a two order of magnitude increase in toughness (1.4–150 J/m^2) [81,82,92,93]. In addition, a carbon contaminant diffused into the interface reduced the G_c value by nearly two orders of magnitude for the thick bonding layer [8,93]. However, a thin 6 nm Cr film used as an adhesive innerlayer for the thin Au film doubled the G_c value from 1.4 to 2.9 J/m^2 [86] as determined from the telephone cord morphology. For these superlayer tests the Ta_2N had a 2.5 GPa compressive residual stress [81,82,86]. While a portion of the as-deposited Ta_2N/Cr/Au system gave telephone cord delamination, a large portion of it did not implying greater adhesion. From the indentation test, these gave G_c values of 9.8 J/m^2 as-deposited and 19.0 J/m^2 fully annealed at 400°C for 16 hours. See Table 2. Thus, while carbon contamination can greatly reduce G_c, a strong innerlayer like Cr promoting adhesion or annealing can double G_c of the Au/Al_2O_3 system.

Copper Films

The most thoroughly studied material has been the Cu/X/SiO_2 system where a range of adhesion has been achieved by varying the innerlayer, the film thickness [22,78,82,85, 88,99] or the test temperature [82]. Initial studies on the single film Cu/SiO_2 system demonstrated that a 40–3000 nm thickness variation could increase the G_c values from about 0.6 to 100 J/m^2. In that same series of studies, the interfacial fracture energies could be increased by about a factor of three using a 10 nm thick innerlayer of titanium [78,82,85]. These studies, utilizing a W superlayer and nanoindentation, are summarized in Table 2 and Figure 15. Also shown there is an upper bound from the previous study [85] and a dislocation free zone, DFZ, model [104] which has been updated as reported in

a later section. Still, these give a good accounting of the increased fracture resistance with an increase in copper thickness. It is clearly seen that the Ti innerlayer increases fracture resistance for all thicknesses by a factor of three. In a similar type of study, Dauskardt. *et al.* [88] also demonstrated an increase in toughness as thicknesses were increased from 30 to 10,500 nm. Here a thin innerlayer of TaN/Ta was utilized to improve adhesion so that the lower limit for the thinner films gave values of about 5 J/m^2. A similar improvement was originally found by Kriese, *et al.* [99,103] using an innerlayer of Cr.

For the first time [82], two sets of data on Cu/SiO_2 interfaces at elevated temperature demonstrate unambiguously that the increase in the work of adhesion increase was due to a plastic energy absorption mechanism. These data eliminated such possibilities as a phase angle change or an increased interfacial strength which could be affected by changing the thickness of the ductile layer. Here for two thicknesses of 80 nm and 500 nm, a range of test temperatures from 80 to 130°C was utilized to evaluate G_c. As is shown in Figures 16(a) and (b), the fracture resistance increased by a factor of four for the thinner film while for the thicker film it increased by more than an order of magnitude. This brittle-to-ductile transition in a normally low-adhesion interface of Cu/SiO_2 with the same Cu thickness and the same bond strength eliminated variables other than the yield strength as possible sources of increased toughening.

Other Systems

Five other systems of importance Nb/Al_2O_3, W/SiO_2, Ta_2N/Al_2O_3, Si_xN_y/SiO_2 and NbN/304SS interfaces are detailed at the bottom of Table 2 [24, 38,46,94,100,103]. The first two clearly demonstrate that for even relatively high strength niobium and tungsten films, that the work of adhesion can be in the 5–10 J/m^2 range if the thickness is 500 nm or greater. The next to last two ceramic/ceramic systems clearly show low adhesion values in the vicinity of 0.5 to 1.5 J/m^2 even though the thickness might be as large as 1000 nm. Most importantly, the Ta_2N/Al_2O_3 tests with a six-fold increase in thickness demonstrated a constant work of adhesion independent of thickness. Finally, the last hard coating/ductile substrate system with somewhat larger thickness produces a huge jump in measured toughness [100]. Compared to the ceramic/ceramic results, this cannot be explained by an increased film thickness but is rather a large substrate combination involving plastic energy dissipation.

In summary to this section on thin film adhesion measurements, it is seen that similar increases in adhesion are found by either increasing the bond strength with inner layers or by increasing the test temperature. For the $Cu/X/SiO_2$ system the increase in both cases is about a factor of four for films less than 100 nm thick. Even larger increases in fracture resistance may be obtained by increasing ductile film thicknesses. With regard to Au, Cu, and Nb films on SiO_2 or Al_2O_3 it is seen that strong innerlayers such as Cr, Ta, Ti, and TiN tend to increase the work of adhesion while weakly bonded innerlayers such as C and Ag decrease adhesion. Since Al/Al_2O_3 is already a strong interface, contaminant innerlayers such as Cu or C can substantially decrease the true work of adhesion.

Given these findings, it is next appropriate to review very briefly some fracture models wherein the important variables with respect to adhesion are included. These include phase angle, yield strength, modulus, thickness and test temperature.

TOUGHENING MECHANISMS

Consider first the influence of the phase angle where Hutchinson and Suo [16,105] have shown that toughness could increase substantially for more opening mode I cracks incorporating more mode II character. Here, the phase angle captures that characteristic, as given by

$$\psi = \tan^{-1}\left(\frac{\tau}{\sigma}\right) \tag{47}$$

where τ is the local shear stress and σ is the local normal stress. The greater the mode II contribution the greater the ratio of τ/σ and thus the greater the phase angle. This ratio can increase several ways, by increasing the far-field applied shear stresses compared to the normal stresses or by increasing the local ratio through the bimaterial modulus effect. As shown through Eqs. (7)–(12) an increase in ψ could substantially increase interfacial toughness. However, in the two extensive studies by Volinsky, *et al.* [78,82,85] and Dauskardt, *et al.* [88] the phase angles of the former [78] after buckling were less than the phase angle of the four-point UCSB test [88], e.g. 10–15° versus 43°. Nevertheless, the toughness measured for both Al/SiO_2 and $Cu/Ti/SiO_2$ versus $Cu/TaN/Ta/SiO_2$ were similar as shown in Figure 14 for Al and now for Cu in Figure 17. If anything, the phase angle effect should give G_c values for the four-point bending test higher than the

superlayer-indentation test. For this reason we discount the phase angle effect as being the major contributor for increased toughness with increasing film thickness or test temperature. Given a single material, it is also clear that modulus is independent of thickness and over the small range of temperatures investigated independent of test temperature. This leaves yield strength, film thickness and test temperature as the three strongly obvious external variables influencing adhesion although there are a host of intrinsic ones such as bond strength, microstructure, etc. that also contribute.

Two early models which could address failure mechanisms in relatively thin films were by Hsia, Suo and Young [106] and by Tvergaard and Hutchinson [83]. These, respectively, gave

$$K_c = \frac{\mu\sqrt{h}\pi\sqrt{\pi}(1-\nu)[\sigma_c/\mu]^2 \ln(h/b)}{\left\{\ln(h/b) - \frac{3}{2}\right\}^2} \tag{48a}$$

$$G_c = K_c^2/E \tag{48b}$$

where σ_c/μ is the ratio of the cohesive strength to shear modulus, h is the film thickness, b is the Burgers vector and ν, E are elastic constants, while for the second model

$$G_c = \Gamma_{SS} = \Gamma_i + 3\pi C_\perp \frac{\sigma_{ys}^2 h}{E} \tag{49}$$

where Γ_{SS} is the steady state resistance and $C_\perp$ is a constant. The first of these is a dislocation shielding model which predicts brittle fracture in a confined film between two constraining layers as in the four-point bend test. The second of these addresses ductile fracture at a film-substrate interface. Neither of these were quite applicable to the interface debonding problem as σ_c was the cohesive strength in (48a) and the only length scale in either is the film thickness. Still with realistic values of σ_c, μ and σ_{ys} Eqs. (48a) and (49) can be shown to fit the data in Figure 14 to first order. Improvements to the dislocation shielding model were suggested by Mao *et al.* [107,108] by taking into account blunting and placing the crack-tip at the interface while Suo, Shih and Varias [109] and Wei and Hutchinson [77] have combined concepts of the elastic zone and the embedded process zone models to add additional length scales. Just one of these, for example, suggests that

$$\Gamma_{SS}/\Gamma_i = F\left[\frac{\hat{\sigma}}{\sigma_{ys}}, N, \frac{\ell}{R_0}\right] \tag{50}$$

where $\hat{\sigma}$ is a peak local stress like σ_c above except at the interface, N is a strain hardening exponent and ℓ/R_0 is a ratio of two length scales, the first associated with strain-gradient plasticity theory and the second the plastic zone size. As none of these explicitly address microstructure, a third process zone length scale has been suggested which considers the length over which separation occurs. How to incorporate these various length scales is still in its infancy and the measuring of such scales except for the plastic zone size is equally difficult.

Taking a somewhat simpler view, we had previously described a brittle to ductile transition model [104,110] for application to cleavage in single crystals and later applied this to thin film fracture [82]. While this is also to first order, it has the parameters of yield strength and length scales with origins in the Rice-Thomson failure criterion [111]. In Thomson's original dislocation emission criterion,

$$k_I = \frac{3}{\pi}\sqrt{\frac{2}{\pi}}\sigma_{ys}\sqrt{c}\left[\ln\left(\frac{4R_p}{c}\right) + \frac{4}{3}\right] \tag{51}$$

where k_I is a local stress intensity, c is the distance between the crack tip and the nearest dislocation and R_p is the plastic zone size. As shown elsewhere [82], by describing the plastic zone size in terms of the far-field applied stress intensity this gives

$$K_c = \frac{\sigma_{ys}c^{1/2}}{2.44}\ \exp\left\{\frac{k_{IG}}{1.52\sigma_{ys}c^{1/2}}\right\} \tag{52}$$

where for an interface K_c would be associated to G_c through (48b) and k_{IG} would be the local Griffith value associated with the true work of adhesion of the interface. While Eq. (52) does have the yield strength, a length scale and a failure criterion (k_{IG}) it does not explicitly include film thickness, h. This however, is implicit as to how film thickness affects yield strength through Eqs. (43), (45) and (46). We have calculated values of k_{IG} and c from available data as reported in Table 3. With the length scale c, as in Eqs. (51) and (52), being linearly related to $(k_{IG}/\sigma_{ys})^2$ in Figure 18 for the yield strength calculated at $h =$ 100 nm, the data suggest that $K_c \sim 3.3\sigma_{ys}c^{1/2}$ at this thickness where plasticity is absent or negligible. This allowed two estimates for determining G_0 through (48b) by taking

K_c^2/E at a film thickness of 100 nm or using k_{IG}^2/E directly.† As these were comparable. the latter are shown in Table 3. Where possible we compared these to the thermodynamic works of adhesion, W_{ad}, as determined from high temperature measurements [95–98] in Figure 19. Except for two relatively high and low points, the comparison is favorable with G_0 values only slightly higher than the thermodynamic adhesion values. Note that in Table 2 we have taken a few liberties in assuming that a TiW interface (which is mostly titanium) with SiO_2 is similar to a Ti/SiO_2 interface and that TaN/SiO_2 would be similar to TiN/SiO_2. Even without these, however, the agreement is encouraging.

Finally, to illustrate the predictive qualities of these models, we have included a comparison of these to the aluminum data of Figure 14. Beyond the critical thickness, G_0 increases to G_c due to plastic energy dissipation. It is seen that all three qualitatively and even quantitatively within adjustable bounds predict the correct trend. Similarly the data for copper in Figure 17 are predicted to first order as shown. Taking the same value of $c = 17$ nm for both 80 nm and 500 nm films as was used for Figure 17, it is seen in Figure 16 that the brittle-to-ductile transition can be predicted as a function of test temperature. The only variable used here was that of test temperature as to how it changed yield strength in Eq. (52). To summarize, this relatively simple three-parameter model with a single flow parameter, σ_{ys}, a single failure criterion, $k_{IG} \equiv \sqrt{EG_0}$, and a single length scale, c, predict both the thickness and temperature dependencies of K_c and therefore G_c, the practical work of adhesion.

Note added in proof: After the experimental work associated with superlayer-indentation was completed and analyzed, it came to our attention that focused-ion beam machining (FIB) was available. Several cross sections of Cu/SiO_2 interfaces indented at

† Note that as Eqs. (51) and (52) are in terms of the local resistance to crack growth that the implicit assumption here is that $G_0 = R$. It should be emphasized here that for some of the data calculations in Table 3 required G_0 to be estimated to know k_{IG} so that c could be determined from Eq. (52). In these cases this becomes a circular argument but in the majority independent determinations were possible. In the others, self-consistency is maintained with the resulting correlation shown in Figure 18.

low, intermediate and high loads were evaluated [112]. As seen in Figure 20(a), the indentation at low load did not trigger delamination. In 20(b), a relatively large load plastically deformed the tungsten and pinned the regions between the crack right under the indenter and those extending further out on both sides to produce the blister. There is about a 500 nm hiatus in cracking on both sides of the central crack. Even though the film was only 120 nm thick, this resulted in a double buckling mode. Finally, in a third indent, it is seen in Figure 3(c) that single buckling results. At the center of original indent, it is now seen that the crack opening is greatest. Compare these with the schematics shown in Figure 6.

SUMMARY

Some twelve thin film or interfacial adhesion tests are reviewed with emphasis toward ductile, thin metallic films. In addition 25 single and multi-film stacks on silicon or alumina substrates are reviewed as to how variations in thickness, chemistry and temperature affect adhesion. Major roles are shown for thickness, test temperature and interface chemistry as to how they affect yield strength and the thermodynamic work of adhesion. For Al, Cu and Au films, any one of these variables are shown to change the practical work of adhesion by an order of magnitude or more. At low thickness, the adhesion asymptotically approaches the thermodynamic work of adhesion while large thickness predominantly controls the practical work of adhesion through plastic energy dissipation. It is shown that resistance-based models need yield strength, a failure criterion and at least one length scale for predictive quality.

ACKNOWLEDGMENTS

The authors would like to acknowledge support for this work by the Center for Interfacial Engineering at the University of Minnesota under grant NSF/CDR-8721551 and the Department of Energy under DOE contract DE-FG02/96ER45574. A.A. Volinsky and N.R. Moody also acknowledge support through DOE contract DE-AC04-94AL85000. The assistance of N.I. Tymiak, B.E. Mills, D.E. McLean and D. Medlin is appreciated. The assistance of Dr. J.C. Nelson from the Center for Interfacial Engineering and Microtechnology Laboratory staff at the University of Minnesota is also gratefully appreciated.

REFERENCES

1. P.A. Steinmann and H.E. Hintermann, *J. Vac. Sci. Tech.* **A7** (1989) p. 2267.
2. M. Ohring, *The Materials Science of Thin Films*, Academic Press Inc. (1991) p. 444.
3. A. Pocius, *Adhesion and Adhesives Technology. An Introduction*, Hanssser Publishers (1997).
4. A.A. Griffith, *Phil. Trans. Roy. Soc. London* **A221** (1920) p. 163.
5. E. Orowan, *Trans. Isntn. Engrs. Shipbuilders Scot.* **89** (1945) p. 89.
6. R.M. Pilliar and J. Nutting, *Phil. Mag.* **16** (1967) p. 181.
7. I. Reimanis, B.J. Dalgleish, M. Rühle and A.G. Evans, *Acta Metall.* **38** (1990) p. 2645.
8. D.M. Lipkin, D.R. Clarke and A.G. Evans, *Acta Mater.* **46**, No. 13 (1998) p. 4835.
9. C. Lee and K. Lin, *Japan J. Appl. Phys.* **33** (1994) p. 2684.
10. A. Furuya, N. Hosoi and Y. Ohshita, *J. Appl. Phys.* **78**, No. 10 (1995) p. 5989.
11. M.L. Jokl, V. Vitek and C.J. McMahon, *Acta Metal.* **28** (1980) p. 1479.
12. K.M. Liechti and Y.S. Chai, *J. Appl. Mech.* **59** (1992) p. 295.
13. H.C. Cao and A.G. Evans, *Mech. Mater.* **7** (1989) p. 295.
14. J.S. Wang and Z. Suo, *Acta Metall. Mater.* **38** (1990) p. 1279.
15. H.M. Jensen and M.D. Thouless, *Int. J. Solids Structs.* **30** (1993) p. 779.
16. J. Hutchinson and Z. Suo, *Adv. Appl. Mech.* **29** (1992) p. 63.
17. J. Dundurs, *J. Appl. Mech.* **32** (1965) p. 400.
18. J.R. Rice, Proceedings of the 1st International Conference on Fracture, Sendai, Japan, T. Yokobuki, T. Kawasaki and J.L. Swedlow, eds., (1966) p. 309.
19. D.M. Lipkin and G.E. Beltz, *Acta Mater.* **44** (1996) p. 1287.
20. D.M. Lipkin, D.R. Clarke and G.E. Beltz, *Acta Mater.* **44** (1996) p. 4051.
21. A. Bagchi, G. Lucas, Z. Suo and A. Evans, *J. Mater. Res.* **9** No. 7 (1994) p. 1734.
22. A. Bagchi and A. Evans, *MRS Symp. Proc.* **383** (1995) p. 183; A. Bagchi and A. Evans, *Thin Solid Films* **286** (1996) p. 203.
23. A. Kinbara, E. Kusano, T. Kamiya, I. Kondo and O. Takenaka, *Thin Solid Films* **317** (1998) p. 165.
24. H. Ji, G.S. Was and M.D. Thouless, *Engng. Fract. Mech.* **61** (1998) p. 163.

25. G. Xu, M.-Y. He and D.R. Clarke, *Acta Mater.* **47**, No. 15 (1999) p. 4113.
26. A.V. Zhuk, A.G. Evans and J.W. Hutchinson, *J. Mater. Res.* **13**, No. 12 (1998) p. 3555.
27. W.C. Oliver and G.M. Pharr, *J. Mater. Res.* **7** (1992) p. 1564.
28. A.G. Evans and J.W. Hutchinson, *Int. J. Solids Structs.* **20**, No. 5 (1984) p. 455.
29. D.B. Marshall and A.G. Evans, *J. Appl. Phys.* **56** (1984) p. 2632.
30. L.G. Rosenfeld, J.E. Ritter, T.J. lander and M.R. Lin, *J. Appl. Phys.* **67**, No. 7 (1990) p. 3291.
31. M.P. de Boer and W.W. Gerberich, *Acta Mater.* **44**, No. 8 (1996) p. 3169.
32. M.P. de Boer and W.W. Gerberich, *Acta Mater.* **44**, No. 8 (1996) p. 3177.
33. M.P. de Boer, PhD Dissertation, University of Minnesota (1996).
34. J.J. Vlassak, M.D. Drory and W.D. Nix, *J. Mater. Res.* **12**, No. 7 (1997) p. 1900.
35. M.D. Drory and J.W. Hutchinson, *Proc. Roy. Soc. London* **A452** (1996) p. 2319.
36. A.A. Volinsky, J.C. Nelson and W.W. Gerberich, *Mater. Res. Soc. Proc.* **563** (1999) p. 397.
37. M.R. Begley, D.R. Mumm, A.G. Evans and J.W. Hutchinson, *Acta Mater.* **48** (2000) p. 3211.
38. J.M. Sanchez, S. El-Mansy. B. Sun. T. Scherban, N. Fang, D. Pantuso, W. Ford, M.R. Elizalde, J.M. Martinez-Escanola, A. Martin-Meizoso, J. Gil-Sevillano, M. Fuentes and J. Maiz, *Acta Mater.* **4**, No. 17 (1999) pp. 4405-4413.
39. M.D. Kriese and W.W. Gerberich, *J. Mater. Res.* **14**, No. 7 (1999) p. 3007.
40. A.A. Volinsky, N.R. Moody and W.W. Gerberich, *Mater. Res. Soc. Proc.* **594** (2000) p. 383.
41. S.P. Timoshenko, *Theory of Elastic Stability*, McGraw-Hill (1961).
42. P. Benjamin and C. Weaver, *Proc. Roy. Soc. London* **A254** (1960) p. 163.
43. P. Burnett and D. Rickersby, *Thin Solid Films* **154** (1987) p. 403.
44. S. Venkataraman, D. Kohlstedt and W.W. Gerberich, *J. Mater. Res.* **8** (1993) p. 685.
45. S. Venkataraman, D. Kohlstedt and W.W. Gerberich, *J. Mater. Res.* **7** (1992) p. 1126..
46. N.R. Moody, R. Hwang, S. Venkataraman, J. Angelo, D. Norwood and W.W. Gerberich, *Acta Mater.* **46**, No. 2 (1998) p. 585.

47. M.P. de Boer, M. Kriese and W.W. Gerberich, *J. Mater. Res.* **12**, No. 10 (1997) p. 2673.

48. M.P. de Boer, J.C. Nelson and W.W. Gerberich, *J. Mater. Res.* **13**. No. 4 (1998) p. 1002.

49. J. Vlassak and W. Nix, *J. Mater. res.* **7**, No. 6 (1992) p. 3242.

50. M.K. Small, J. Vlassak and W. Nix, *MRS Symp. Proc.* **239** (1992) p. 257.

51. M.K. Small and W.D. Nix, *J. Mater. Res.* **7**, No. 6 (1992), p. 1553.

52. V. Paviot, J. Vlassak and W. Nix, *MRS Symp. Proc.* **356** (1995) p. 579.

53. R. Hohfelder, H. Luo, J. Vlassak, C. Chidsey and W. Nix, *MRS Symp. Proc.* **436** (1997) p. 115.

54. A.A. Volinsky, unpublished work.

55. K.-T. Wan and S.-C. Lim, *Int. J. Fract.* **92** (1998) p. 43.

56. H.M. Jensen, *Int. J. Fract.* **94** (1998) p. 79.

57. *ASTM Standard 399-90* (1990) p. 407.

58. Z. Suo and J.W. Hutchinson. *Mater. Sci. Engng.* **A107** (1989) p. 135.

59. M. Menningen and H. Weiss, *Surf. Coatings Tech.* **76-77** (1995) p. 835.

60. J.M. McNaney, R. Havens and R.O. Ritchie, *J. Testing & Eval.* **23** (1995) p. 28.

61. J.M. McNaney, R.M Cannon and R.O. Ritchie, *J. Testing & Eval.* **23** (1995) p. 95.

62. M.F. Kanninen, *Int. J. Fract.* **9** (1973) p. 83.

63. H.C. Cao, B.J. Dalgleish and A.G. Evans, *Closed Loop* **17** (1989) p. 19.

64. N. O'Dowd, C. Shih and M. Stout, *Int. J. Solids Structs.* **29**, No. 5 (1992) p. 571.

65. C. Atkinson, R. Smelser and J. Sanchez, *Int. J. Fract.* **18**, No. 4 (1982) p. 279.

66. D. Shetty, A. Rosenfield and W. Duckworth, *Engng. Fract. Mech.* **26**, No. 6 (1987) p. 825.

67. Y. Huang, C. Liu and MG. Stout, *Acta Mater.* **44**, No. 3 (1996) p. 1223.

68. J. Wang and Z. Suo, *Acta Metall. Mater.* **38**, No. 7 (1990) p. 1279.

69. P.G. Charalambides, J. Lund, A.G. Evans and R.M. McMeeking, *J. Appl. Mech.* **111** (1989) p. 77.

70. I. Hofinger, M. Oechsner, H. Bahr and M. Swain, *Int. J. Fract.* **92** (1998) p. 213.

71. R.H. Dauskardt, M. Lane, Q. Ma and N. Krishna, *Engng. Fract. Mech.* **61** (1998) p. 141.

72. T.L. Becker, Jr., J.M. McNaney, R.M. Cannon and R.O. Ritchie, *Mech. of Mater.* **25** (1997) p. 291.

73. T.P. Weihs, S. Hong, J.C. Bravman and W.D. Nix, *J. Mater. Res.* **3**, No. 5 (1988) p. 931.

74. S.P. Baker and W.D. Nix, *J. Mater. Res.* **9**, No. 12 (1994) p. 3131.

75. S.P. Baker and W.D. Nix, *J. Mater. Res.* **9**, No. 12 (1994) p. 3145.

76. D. Kramer, H. Huang, M. Kriese, J. Robach, J. Nelson, A. Wright, D. Bahr and W.W. Gerberich, *Acta Mater.* **47** (1999) p. 333.

77. Y. Wei and J.W. Hutchinson, *J. Mech. Phys. Solids* **45** (1997) p. 1137.

78. N. Tymiak, A.A. Volinsky,M.D. Kriese, S.A. Downs and W.W. Gerberich, *Met. Mater. Trans. A* **31A** (2000) p. 863.

79. R.P. Vinci, E.M. Ziplinski and J.C. Bravman, *Thin Solid Films* **262** (1995) p. 142.

80. R. Venkataraman and J.C. Bravman, *J. Mater. Res.* **7**, No. 8 (1992) p. 2040.

81. A.G. Evans, J.W. Hutchinson and Y. Wei, *Acta Mater.* **47**, No. 15 (1999) p. 4093.

82. W.W. Gerberich, A.A. Volinsky, N.I. Tymiak and N.R. Moody, *Mater. Res. Soc. Proc.* **594** (2000) p. 351.

83. V. Tvergaard and J.W. Hutchinson, *J. Mech. Phys. Solids* **44**, No. 5 (1996) p. 789.

84. M.R. Turner and A.G. Evans, *Acta Mater.* **44**, No. 3 (1996) p. 863.

85. A.A. Volinsky, N.I. Tymiak, M.D. Kriese, W.W. Gerberich, J.W. Hutchinson, MRS Symp. Vol. 539 (1999) p. 277.

86. N.R. Moody, D.P. Adams, A.A. Volinsky, M.D. Kriese and W.W. Gerberich, "Annealing Effects on Interfacial Fracture of Gold-Chromium Films on Hybrid Microcircuits," MRS Symp. on "Optimization of Interfaces," Fall 1999 MRS, in press.

87. J.A. Schneider, S.E. Guthrie, M.D. Kriese, W.M. Clift and N.R. Moody, *Mat. Res. Soc. Symp. Vol.* **522** (1998) p. 347.

88. M. Lane and R.H. Dauskardt. *J. Mater. Res.* **15**, No. 1 (2000) p. 203.

89. D.F. Bahr, J.W. Hoehn, N.R. Moody and W.W. Gerberich, *Acta Mater.* **45**(12) (1997) p. 5163.

90. N.R. Moody, S.K. Venkataraman, R.Q. Hwang, J.E. Angelo and W.W. Gerberich. *Corrosion/Deformation Interactions*, T. Magnin, ed., *Eur. Fed. Corros. Publ.* **21** (1997)pp. 227.

91. M. Lane, A. Vainchtein, H. Gao and R.H. Dauskardt, *J. Mater. Res.* **16** (2001) in press.

92. I.E. Reimanis, *Acta Mater.* **46**, No. 7 (1998) p. 2479.

93. D.M. Lipkin, D.R. Clarke and A.G. Evans, *Acta Mater.* **46**, No. 13 (1998) p. 4835.

94. H. Ji, G.S. Was and M.D. Thouless, *Mat. Res. Soc. Symp. Vol.* **522** (1998) p. 325.

95. M.G. Nicholas, in *Surfaces and Interfaces of Ceramic Materials*, L.C. Dufour, *et al.*, eds., Kluwer Acad. Press, Norwell, MA (1989) p. 393.

96. E.D. Hondros, in *Precip. Processes in Solids*, TMS-AIME, Warrendale, PA (1978) p. 1.

97. R.M. Pilliar and J. Nutting, *Philos. Mag.* **16** (1967) p. 181.

98. J.L. Smialek, D.T. Jayne, J.C. Schaeffer and W.H. Murphy, *Thin Solid Films* **253** (1994) p. 285.

99. M.D. Kriese, N.R. Moody and W.W. Gerberich, *Acta Mater.* **46**, No. 18 (1998) p. 6623.

100. S.V. Hainsworth, M.R. McGurk and T.F. Page, *Surfaces and Coatings Technology* **102** (1998) p. 97.

101. A.A. Volinsky, PhD Thesis, University of Minnesota (2000).

102. W.W. Gerberich, A.A. Volinsky, N.I. Tymiak and N.R. Moody, *Mater. Res. Soc. Proc. Vol.* **594** (2000) p. 383.

103. M.D. Kriese, N.R. Moody and W.W. Gerberich, *J. Mater. Res.* **14**, No. 7 (1999) p. 3019.

104. W. Zielinski, H. Huang, P.G. Marsh and W.W. Gerberich, Part I, II, III, *Acta Metall. et Mater.* **40** (1992) pp. 2861, 2873, 2883.

105. Z. Suo and J. Hutchinson, *Intern. J. Fract.* **43** (1990) p. 1.

106. K.J. Hsia, Z. Suo and W. Yang, *J. Mech. Phys. Solids* **42**, No. 6 (1994) p. 877.

107. S.X. Mao and X.-P. Li, *Philos. Mag. A* **79**, No. 8 (1999) p. 1817.

108. S.X. Mao and M.Z. Li, *J. Mech. Phys. Solids* **47** (1999) p. 2351.

109. Z. Suo, F. Shih and A. Varias, *Acta Metall. Mater.* **41** (1993) p. 1551.

110. H. Huang and W.W. Gerberich, *Acta Metall. Mater.* **42** (1994) p. 639; P.G. Marsh and W.W. Gerberich, *Acta Metall. Mater.* **42** (1994) p. 613.

111. J.R. Rice and R. Thomson, *Philos. Mag.* **29** (1974) p. 73.

112. A.A. Volinsky, M.L. Kottke, I.S. Adhihetty and W.W. Gerberich, "Fiducial Marks as a Measure of Thin Film Crack Arrest Toughness," invited paper, ICF10, December 2001.

FIGURE CAPTIONS

Figure 1. Contact angle measurement schematic.

Figure 2. Interfacial fracture toughness as a function of the mode mixity angle.

Figure 3. Phenomenological functions for $\Gamma(\Psi)$.

Figure 4. Superlayer test schematics.

Figure 5. Film decohesion in the superlayer test.

Figure 6. a) No buckling during indentation; b) double-buckling during indentation: c) single-buckling after the indenter tip removal.

Figure 7. Optical micrographs of indentation induced blisters with (right) and without (left) a W superlayer.

Figure 8. Schematic of a bilayer film bending due to the residual stress in each layer.

Figure 9. Schematic of the precracked line scratch test (PLST).

Figure 10. Strain energy release rate for the precracked line scratch test (PLST).

Figure 11. Schematic of unstable crack growth during buckling for PLST.

Figure 12. Bulge test schematic.

Figure 13. Sandwich specimen tests schematics: a) Modified K_{IC} sample; b) Brazil-nut sample; (c) 4-point bent (UCSB) sample.

Figure 14. Increase in strain energy release rate as a function of film thickness from five investigations [71,87,89,(101,102),25] compared to three theoretical models [82, (106,108),109].

Figure 15. Cu film adhesion on different underlayers.

Figure 16. Temperature effects on interfacial toughness for 80 and 500 nm thick Cu films as predicted by Eq. (52), solid curves.

Figure 17. Increase in strain energy release rate as a function of film thickness from two investigations [88,(78,82,85,99)] compared to two theoretical models [82, (106,108)].

Figure 18. Comparison of how the dislocation free zone length scale parameter, c, is related to the interfacial Griffith energy ($k_{IG} = [2E\gamma_i]^{1/2}$) and yield strength.

Figure 19. Direct comparison of G_0 determined at 100 nm film thicknesses to values of the thermodynamic adhesion energy for metal film/SiO_2 or Al_2O_3 interfaces. (Note

that some of these values are back calculated by extrapolating or interpolating the value of K_c at 100 nm.)

Figure 20. FIB cross-sections of the indents into W/Cu 120 nm corresponding to schematic from Figure 6: a) no buckling; b) double-buckling during indentation: c) single-buckling after the indenter tip removal.

TABLE 2: Mechanical properties of the thickest adhering film of interest.

System	Yield, σ_{ys} MPa	Modulus E GPa	Thick h nm	Work of Adhesion G_0 J/m^2	$W_d^{theor.}$	Local Stress intensity, k_{IG} MPa·m$^{1/2}$	T °C	G_c ‡‡ J/m^2	Refs.
Ta†/Al/C/Al_2O_3	298	70	500	0.33	–	0.153	20	1.05	87
W†/Al-Cu/C/SiO_2/Si	298→203	70	500-3200	0.25	–	0.132	20	0.2–0.65	101
W†/Al-Cu/Cu/SiO_2/Si	700→ 203	70	40 3200	0.41		0.17	20	0.3–27	101,102
Ta_2N†/Al/Al_2O_3	190	70	178	-		–	20	7.0	89
SiO_2/TiN/Al-Cu/SiO_2/Si	430→196	70	150-400	5.0	-	0.59	20	4.9–13	71
SiO_2/Al/TiN/Ti/SiO_2		70	250	–	–	–	20	1.9	25
Ta†/Al-Cu/Al_2O_3	298	70	500	–	–	–	20	5.6	87
W†/Al-Cu/SiO_2/Si	329→252	70	340–1000	4.3	–	0.55	20	7.7–8.2	101,102
Au/C/Al_2O_3	338	80.8	15,000	0.317	0.3	0.16	20	1.7	8,84,93
Au/Al_2O_3	338	80.8	15,000	1.27	0.6,0.5	0.32	20	80,230	8,81,84,92,93
TaN†/Au/Al_2O_3	517	80.8	200	0.63	0.6,0.5	0.225	20	1.4	82,86
TaN†/Au/Cr/Al_2O_3	517	80.8	200	1.35	–	0.33	20	2.9	86
	517	80.8	200	–	–		20	(9.8)•••	
	517	80.8	200	–	–	–	20	(19.0)•••	

TABLE 2 (continued)

System	Yield, σ_{ys} MPa	Modulus E GPa	Thick h nm	Work of Adhesion G_0 J/m^2	$W_d^{theor.}$	Local Stress intensity, k_{IG} MPa·m$^{1/2}$	T °C	G_c †† J/m^2	Refs.
W†/Cu/SiO_2/Si	974→466	120	40-3000	0.90	0.8	0.33	20	0.6-100	78,82,85,99
W†/Cu/Ti/SiO_2/Si	974→466	120	40-3000	3.63	2.2*	0.66	20	4-110	10,78,82,85
SiO_2/Cu/TaN/Ta/SiO_2/Si	1060→435	120	30-10,500	5.0	1.8*	0.77	20	4.5-80	10,88
W/Cu/Cr/SiO_2/Si	630→509	120	440-1100	5.3	-	0.8	20	7-15	99,103
W†/Cu/SiO_2Si	806→540	120	80	0.90	0.8	0.33	20-130	1-4.1	82
W†/Cu/SiO_2/Si	560→300	120	500	0.90	0.8	0.33	20-130	14-215(?)	82
Cr†/Cu/SiO_2	913→528	120	50-800	0.5	0.8	0.24	20	0.5-1.0	22
Nb/Al_2O_3	~2000**	103	105	~0.95	0.8	~0.313	-	0.95	24,94-98
Nb/Ag/Al_2O_3	~2000**	103	105	~0.78	0.5	~0.28	-	0.78	24,94-98
W/SiO_2/Si	1220→1088	360	530-760	1.73	-	0.79	20	5.5-9.0	103
Ta_2N/Al_2O_3	-	-	100-600	0.5	-	-	20	0.5-0.5	46
Si_xN_y/SiO_2/Si	-	171	1000	-	-	-	20	1.5	38
NbN/304SS	-	468	2800	-	-	-	-	~400	100

† Used as a superlayer on top of the film of interest.
†† Range refers to the variation with either thickness or temperature.
* Actually TiW and TiN as opposed to Ti and TaN used at the interface as a thin adhesive layer.
** Yield estimated from nanohardness of 6 GPa by $H/3$.
*** Values in ( ) denote values from superlayer indentation on as-deposited (top) and annealed (bottom) films.

TABLE 3: Length scale, c, determinations for 12 different multilayers compared to the normalized Griffith stress intensity squared $(k_{IG}/\sigma_{ys})^2$.

Material Stack	c,* nm	σ_{ys},† MPa	k_{IG},** MPa-m$^{1/2}$	$(k_{IG}/\sigma_{ys})^2$, nm	Ref.
$W/W/SiO_2/Si$	1.45	2500	0.335	18	103
$Nb/Ag/Al_2O_3$	2.2	2000††	0.283	20	24, 94
Nb/Al_2O_3	2.7	2000	0.313	24.5	24, 94
$Au/C/Al_2O_3$	8.0	600	0.16	71	93
Au/Al_2O_3	11	600	0.225	141	86
$Cr/Cu/SiO_2/Si$	11	763	0.24	75	22
$Al/C/SiO_2/Si$	13	494	0.132	71	87
$Al/C/SiO_2/Si$	13	494	0.153	96	87
Au/Al_2O_3	14	600	0.32	284	92,93
$Al/Cu/SiO_2/Si$	15	494	0.17	118	101,102
$Cu/SiO_2/Si$	17	763	0.33	187	88
$Au/Cr/Al_2O_3$	24	600	0.33	303	86
$Cu/Ti/SiO_2/Si$	60	763	0.66	748	78,82,85
$Cu/Cr/SiO_2/Si$	85	763	0.70	840	103
$Al/SiO_2/Si$	300	494	0.55	1240	101,102

† Yield strength at $h = 100$ nm (estimated where necessary).

†† Estimated from $H/3$ at $h = 105$ nm.

* Back calculated from Eq. (52) at $K_c = k_{IG} = \sqrt{EG_0}$ with G_0 from Table 2.

** Determined experimentally from $k_{IG} = K_c$ at a film thickness of 100 nm or with G_0 from Table 2.

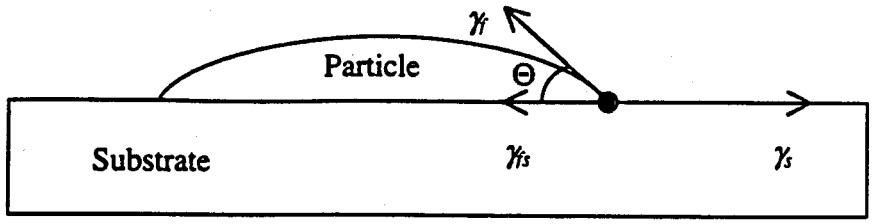

Figure 1. Contact angle measurement schematic.

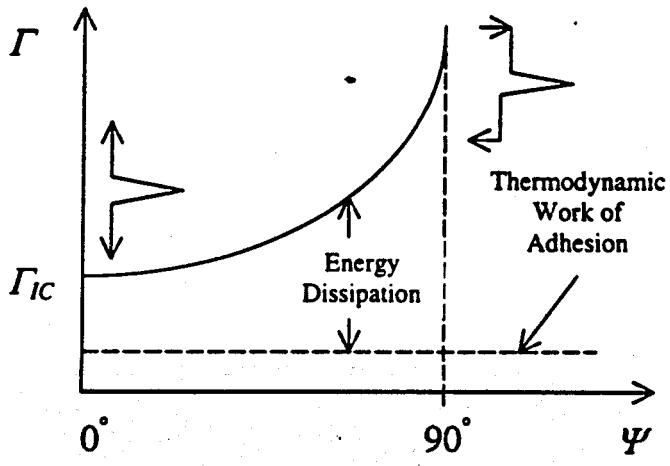

Figure 2. Interfacial fracture toughness as a function of the mode mixity angle.

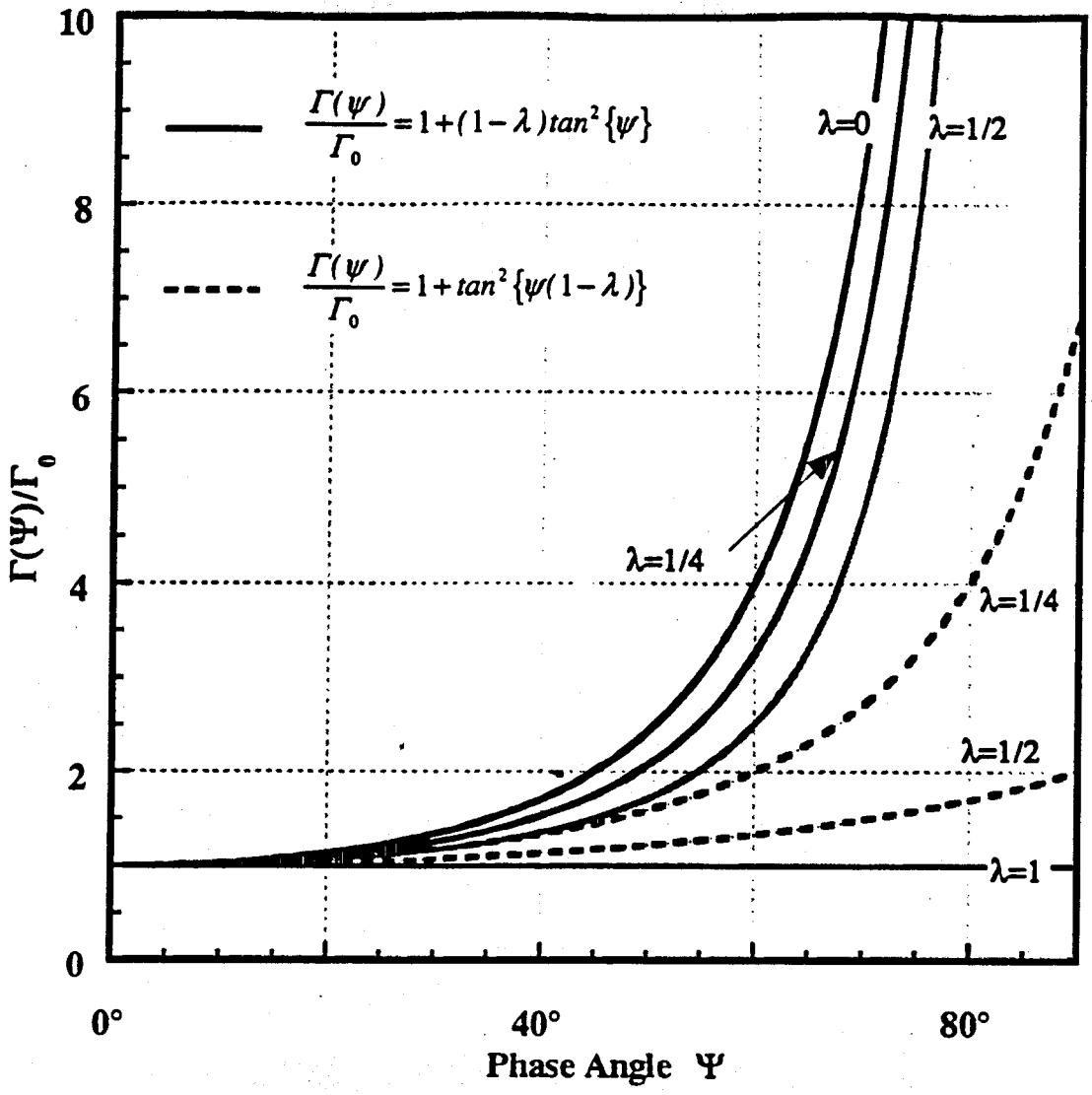

Figure 3. Phenomenological functions for $\Gamma(\psi)$.

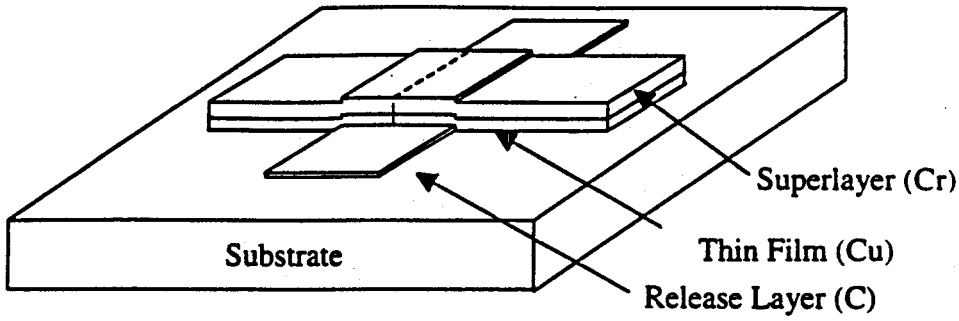

Figure 4. Superlayer test schematics.

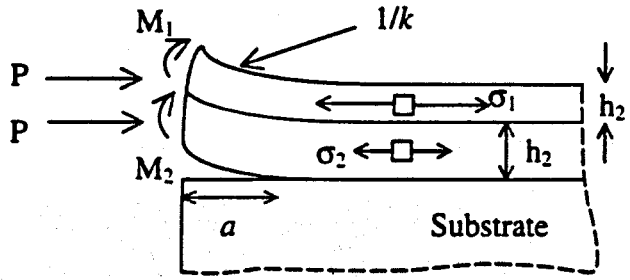

Figure 5. Film decohesion in the superlayer test.

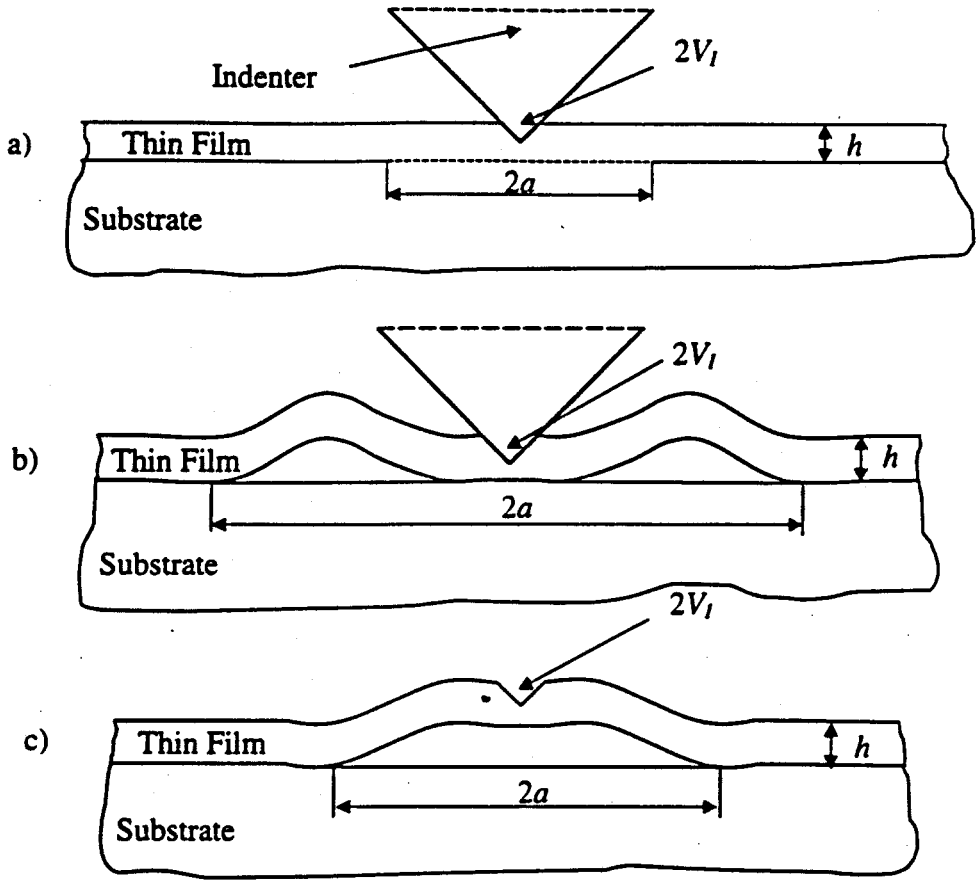

Figure 6. a) No buckling during indentation; b) double-buckling during indentation; c) single-buckling after the indenter tip removal.

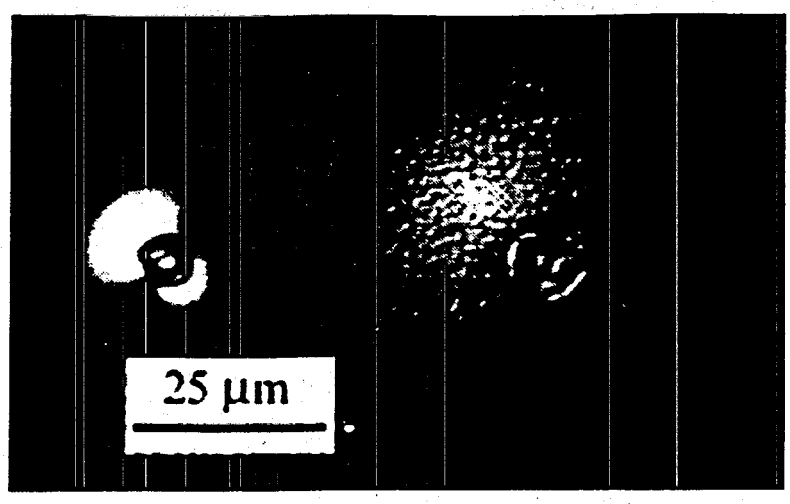

Figure 7. Optical micrographs of indentation iduced blisters with (right) and without (left) a W superlayer.

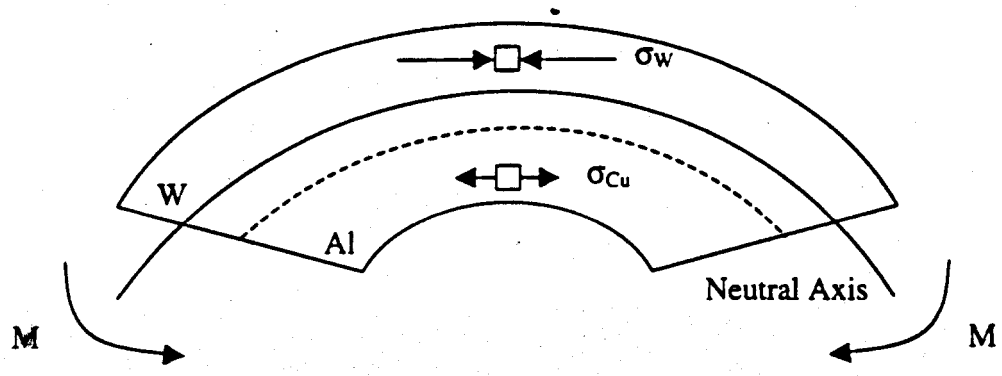

Figure 8. Schematic of a bilayer film bending due to the residual stress in each layer.

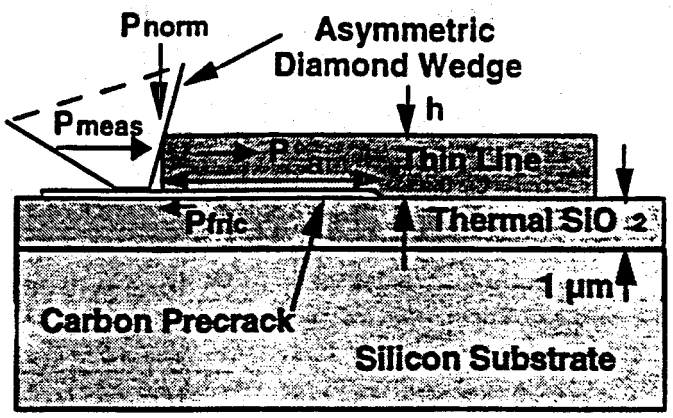

Figure 9. Schematic of the precracked line scratch test (PLST).

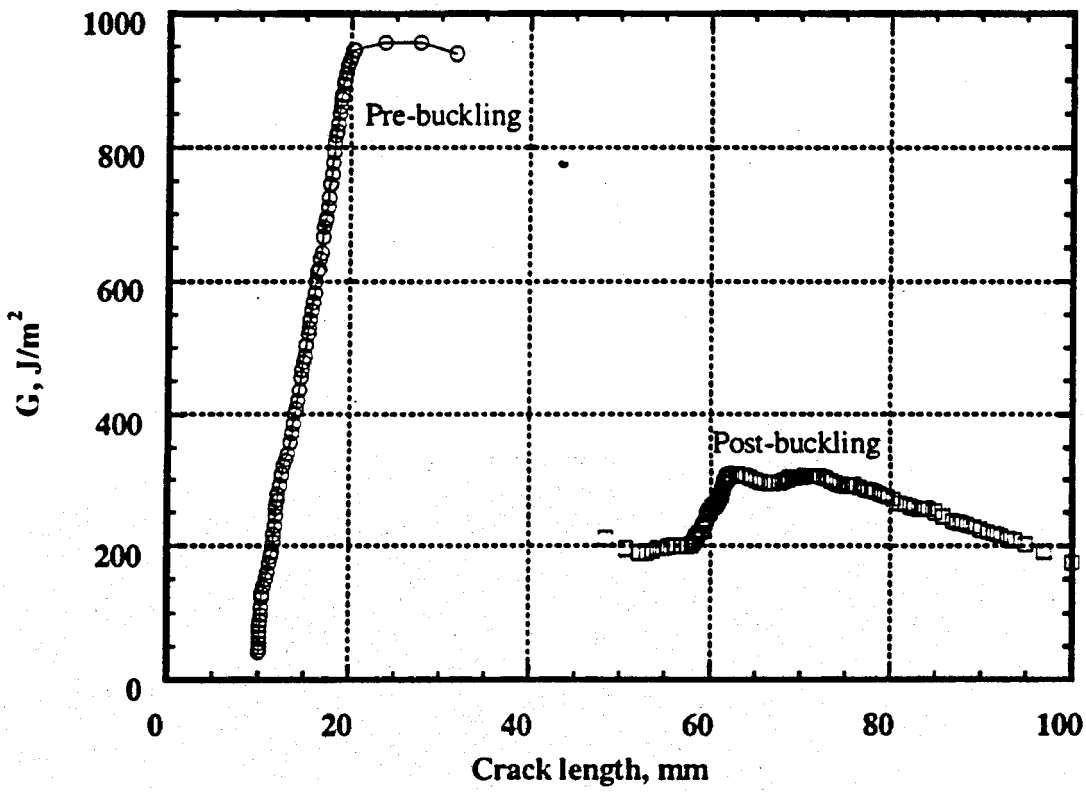

Figure 10. Strain energy release rate for the Precracked Line Scratch Test (PLST).

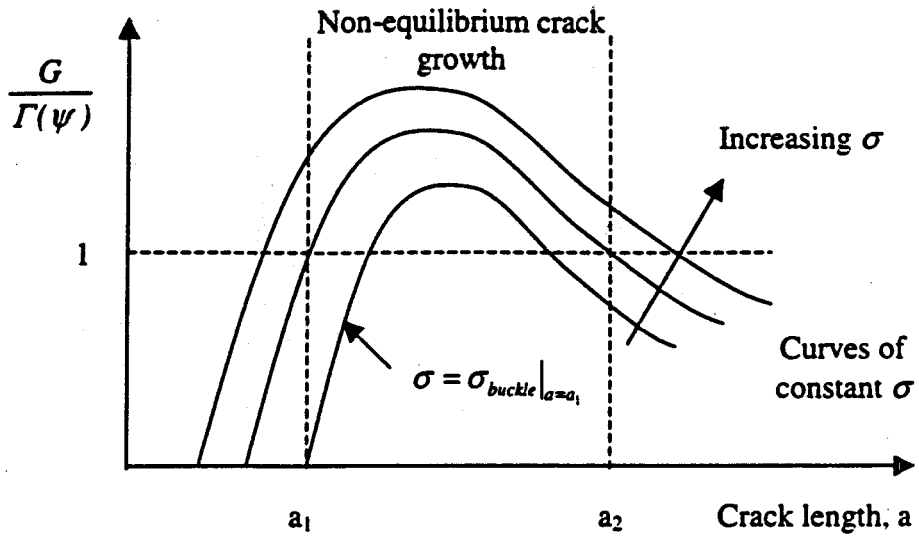

Figure 11. Schematic of unstable crack growth during buckling for the PLST.

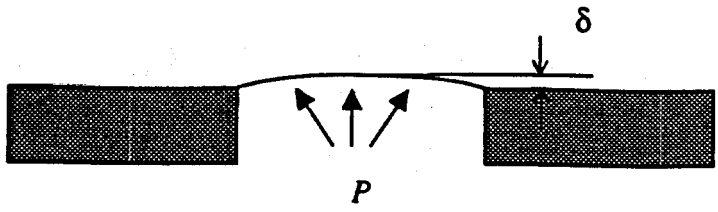

Figure 12. Bulge test schematic.

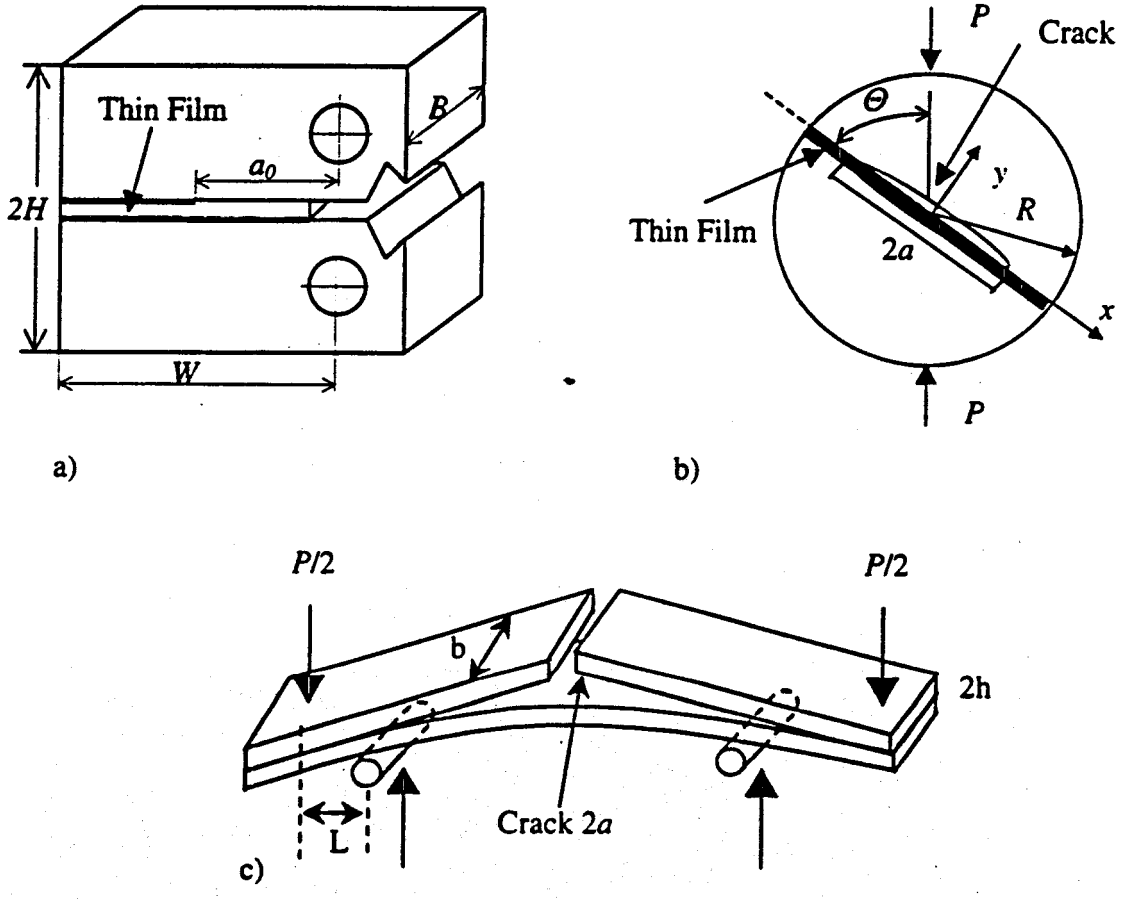

Figure 13. Sandwich specimen tests schematics: a) Modified K_{IC} sample; b) Brazil-nut sample; c) 4-point bent (UCSB) sample.

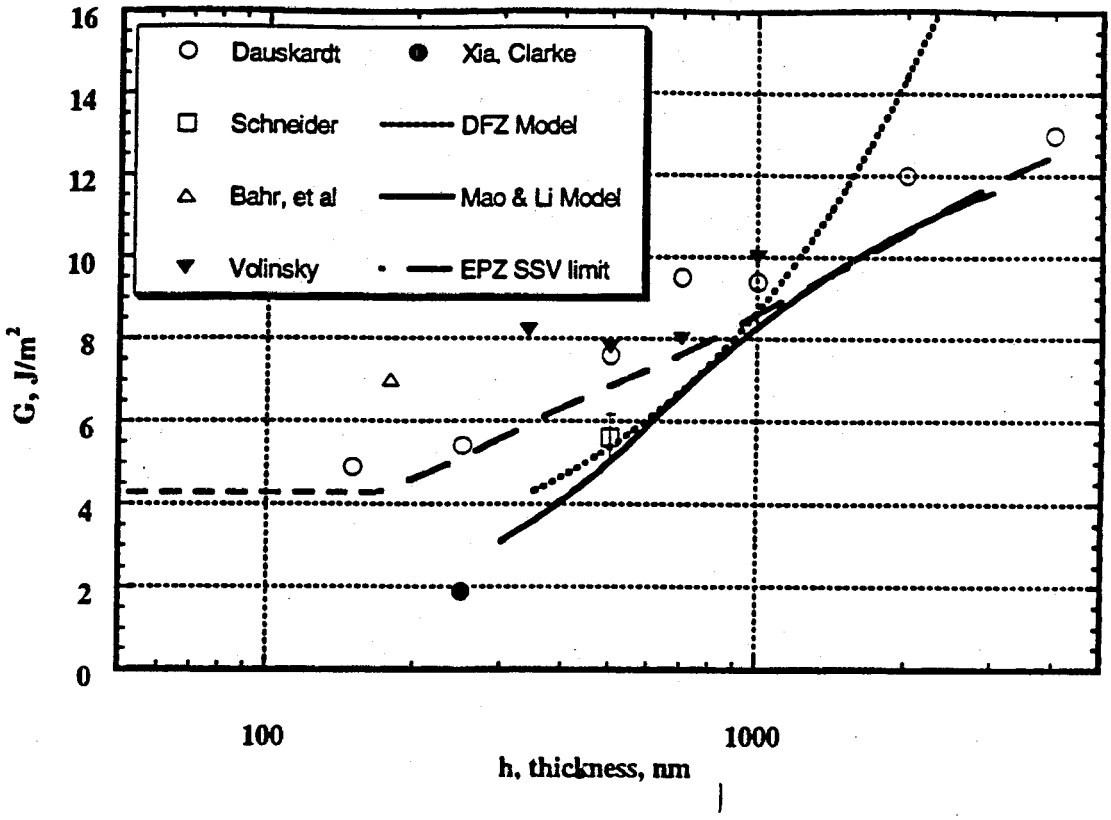
Dauskardt
Xia, Clarke
Schneider
DFZ Model
Bahr, et al
Mao & Li Model
Volinsky
EPZ SSV limit
G, J/m²
h, thickness, nm
0
2
4
6
8
10
12
14
16
100
1000

Figure 14.

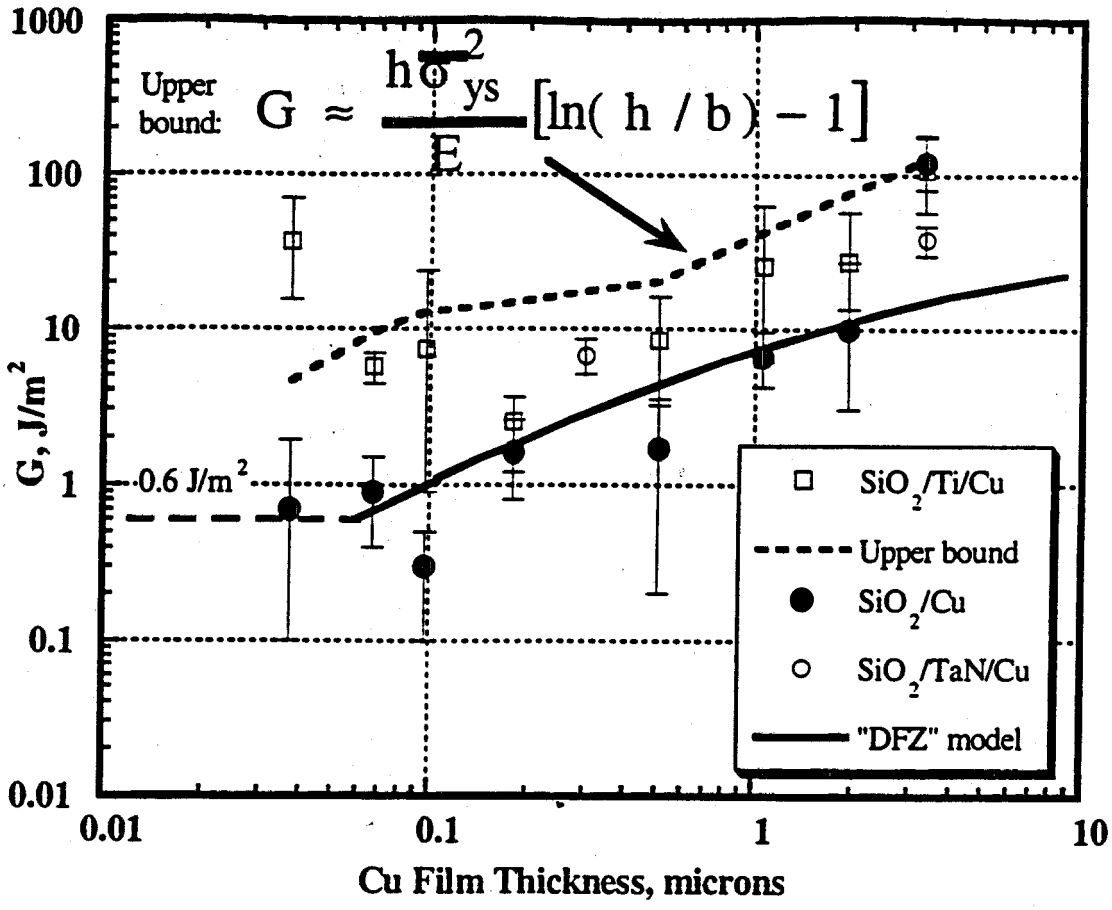

Figure 15. Cu film adhesion on different underlayers.

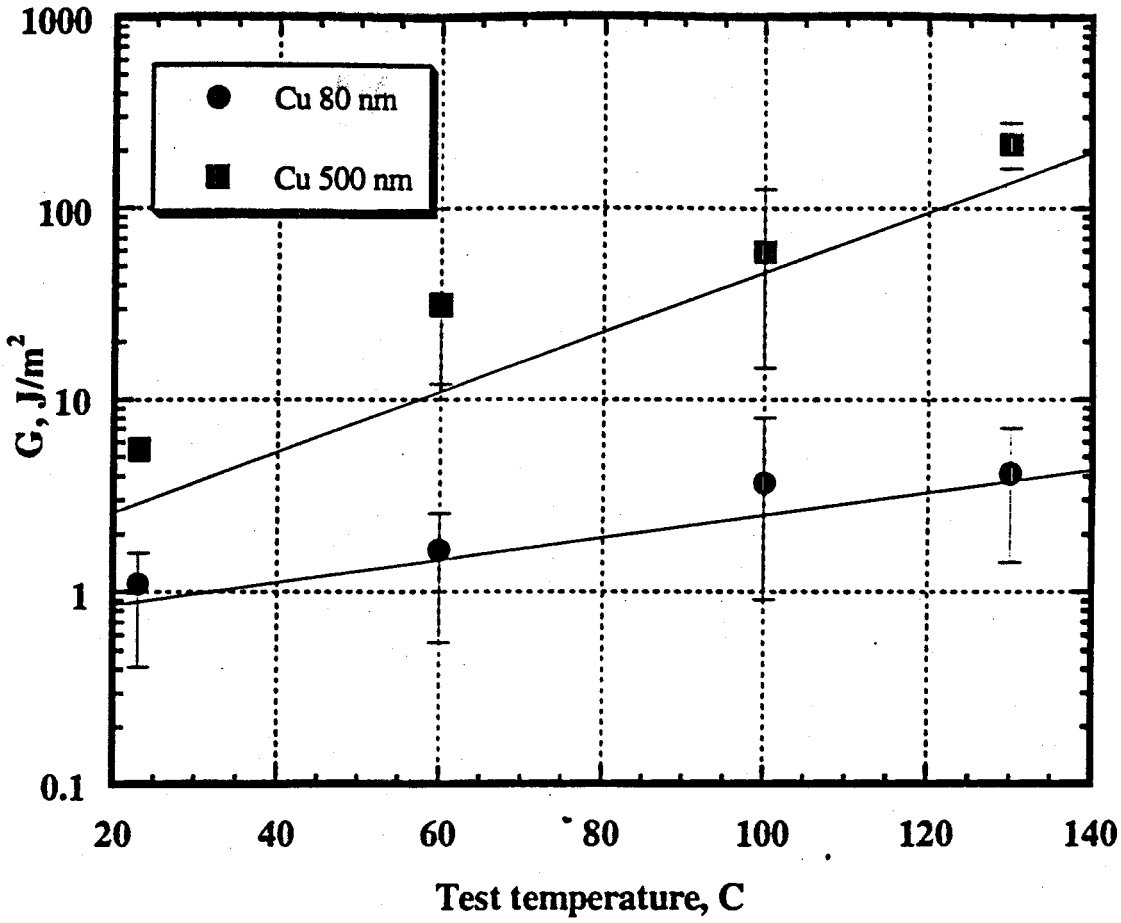

Figure 16: Temperature effects on interfacial toughness for 80 and 500 nm thick Cu films as predicted by Eq. (52), solid curves.

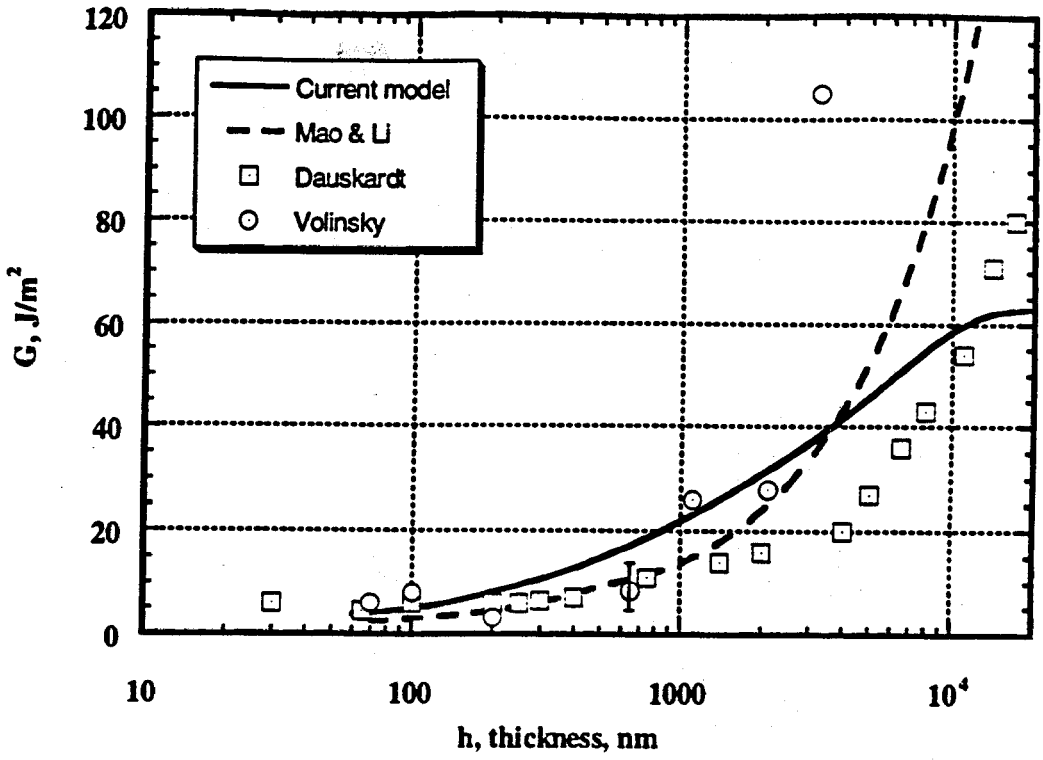
120
100
80
60
40
20
0
G, J/m²
Current model
Mao & Li
Dauskardt
Volinsky
10
100
1000
10⁴
h, thickness, nm

Figure 17.

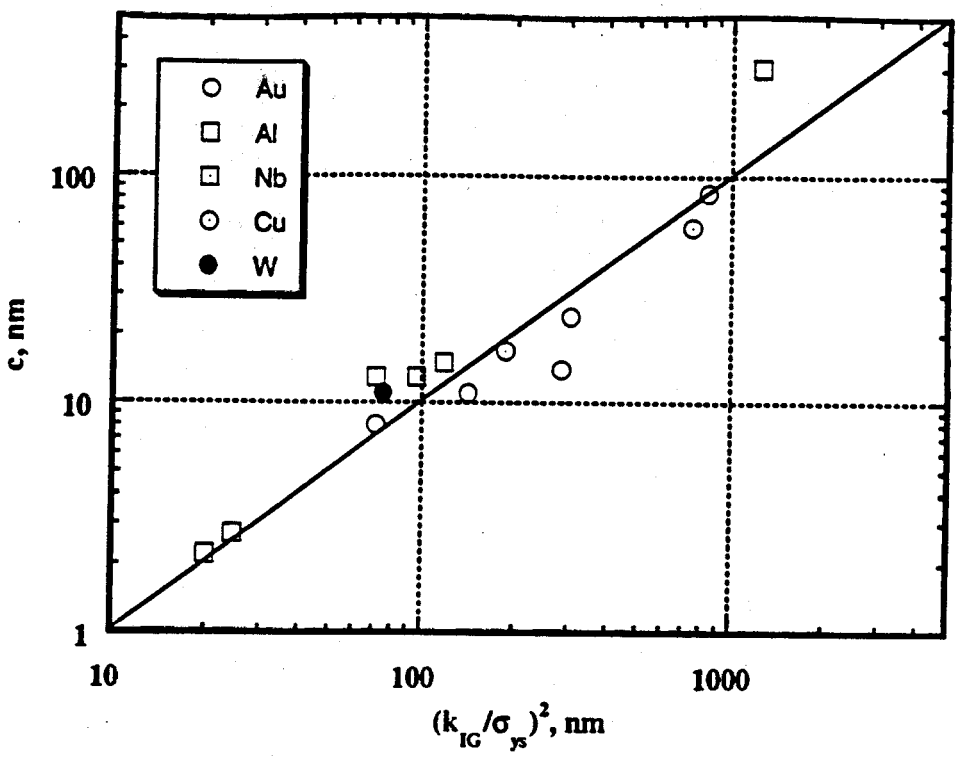

Figure 18.

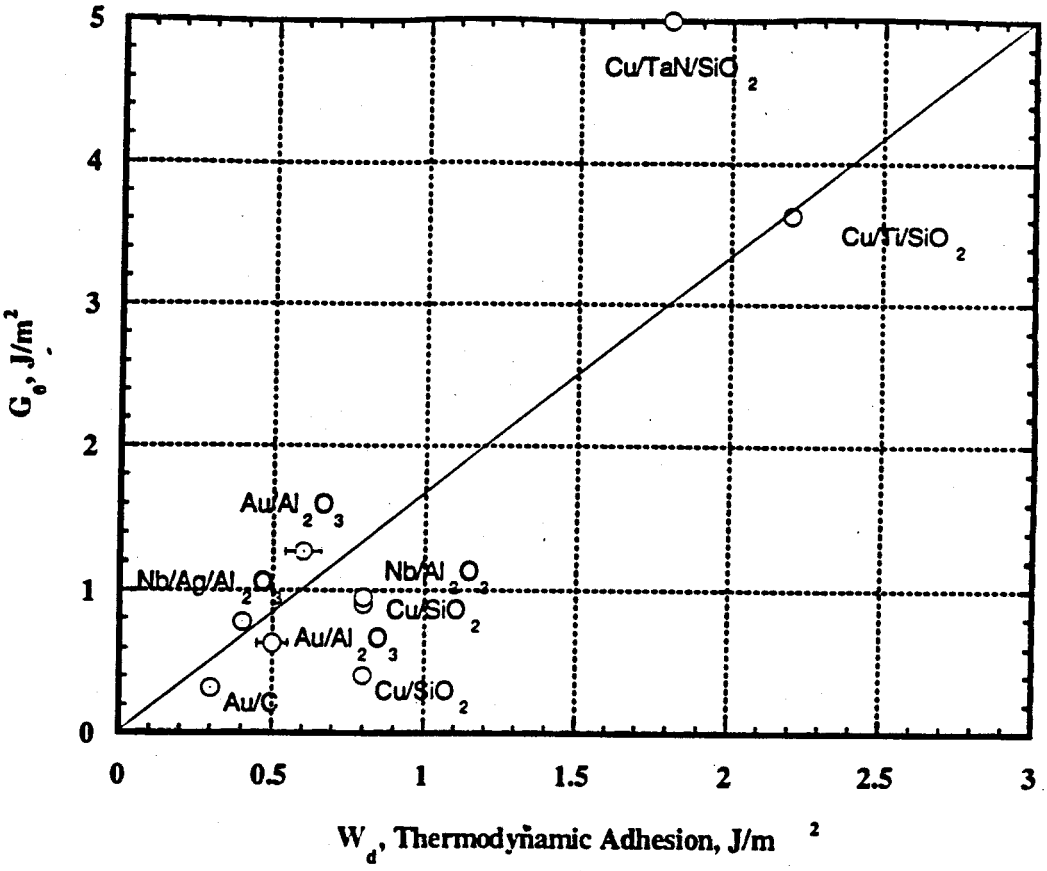
5
4
3
2
1
0
0
0.5
1
1.5
2
2.5
3
G_e, J/m^2
W_d, Thermodynamic Adhesion, J/m^2
Cu/TaN/SiO$_2$
Cu/Ti/SiO$_2$
Au/Al$_2$O$_3$
Nb/Ag/Al$_2$O$_3$
Nb/Al$_2$O$_3$
Cu/SiO$_2$
Au/Al$_2$O$_3$
Au/C
Cu/SiO$_2$

Figure 19.

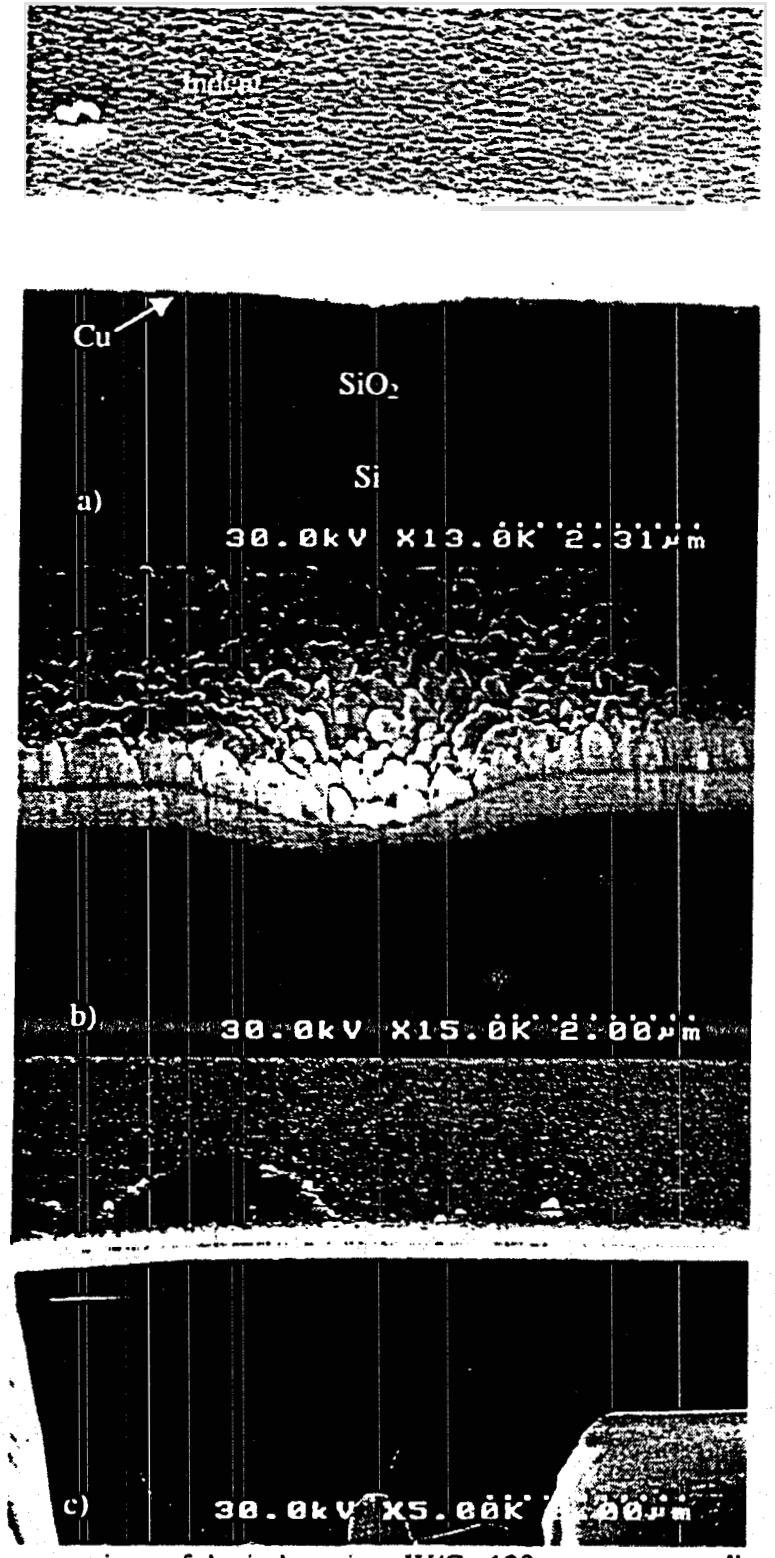

Figure 20. FIB crossections of the indents into W/Cu 120 nm corresponding to schematic from Figure 6: a) No buckling; b) double-buckling during indentation; c) single-buckling after the indenter tip removal.